

FLOW AROUND AXISYMMETRIC AND TWO-DIMENSIONAL  
FORWARD-FACING CAVITIES

Except where reference is made to the work of others, the work described in this thesis is my own or was done in collaboration with my advisory committee. This thesis does not include proprietary or classified information.

---

Rifki

Certificate of Approval:

---

George Flowers  
Professor  
Mechanical Engineering

---

Anwar Ahmed, Chair  
Associate Professor  
Aerospace Engineering

---

Roy J. Hartfield  
Associate Professor  
Aerospace Engineering

---

Stephen L. McFarland  
Acting Dean  
Graduate School

FLOW AROUND AXISYMMETRIC AND TWO-DIMENSIONAL  
FORWARD-FACING CAVITIES

Rifki

A Thesis

Submitted to

the Graduate Faculty of

Auburn University

in Partial Fulfillment of the

Requirements for the

Degree of

Master of Science

Auburn, Alabama  
May 11, 2006

FLOW AROUND AXISYMMETRIC AND TWO-DIMENSIONAL  
FORWARD-FACING CAVITIES

Rifki

Permission is granted to Auburn University to make copies of this thesis at its discretion, upon request of individuals or institutions and at their expense. The author reserves all publication rights.

---

Signature of Author

---

Date of Graduation

## VITA

Rifki, son of Masrif and Zuljasni, was born on April 11, 1979, in Jakarta, the capital of Indonesia. He graduated high school in 1997 and entered Institute of Technology Bandung, West Java, Indonesia. In 2002, he graduated with Bachelor of Science in Aerospace Engineering. After working as a Customer Service Supervisor for Indonesian Airlines, an IT Support for Schlumberger, and a self employed software developer within two years period, he entered Graduate School at Auburn University, in August, 2004.

THESIS ABSTRACT

FLOW AROUND AXISYMMETRIC AND TWO-DIMENSIONAL  
FORWARD-FACING CAVITIES

Rifki

Master of Science, May 11, 2006  
(B.S., Institute of Technology Bandung, Indonesia, 2002)

98 Typed Pages

Directed by Dr. Anwar Ahmed

Flowfield of axisymmetric and two-dimensional forward facing cavities was investigated. Flow visualization results obtained using PLIF and hydrogen bubbles were used to develop a generic flow topology consisting of a combination of vortical structures, foci and a detached primary singular point. Ejection of large eddies from the cavity was closely related to the entrainment and exchange with the outer fluid flow for both types of cavities. Aspect ratio of the cavity had a strong effect on the flow inside the cavity. The primary singular point moved further downstream toward the interior of the cavity with increasing aspect ratio, and was off the geometric centerline due to unsteadiness of the cavity flow structures.

The Reynolds number however had a more pronounced effect on the vorticity and trajectory of the flow structures. Spectral analysis revealed that the shedding of the wake imposed subharmonics disturbances on the upstream flow resulted in the ejection of fluid structures from the cavity. The Strouhal number of the wake of the axisymmetric cavities increased with aspect ratio. The wake of the two-dimensional cavity closely followed classical two-dimensional bluff body wakes with a mean Strouhal number of 0.21.

## ACKNOWLEDGEMENTS

The author would like to thank Dr. Anwar Ahmed for providing him with this opportunity, guidance, support and access to his vast knowledge. The author would also like to thank the committee for this opportunity given to him, Mr. Zafar Bangash for his assistance, Mr. Andy Weldon for making him all the experimental setups that make this work possible, Dr. Jim Lin for his technical support, and the Aerospace Engineering Department of Auburn University for the opportunity and financial support. The author would like to address most of his thanks to his parents for their unlimited support.

Style used: AIAA Journal

Software used: Microsoft Word, Tecplot, Axum, Adobe Photoshop, Solid Edge.



## TABLE OF CONTENTS

LIST OF FIGURES .....	xi
NOMENCLATURE .....	xvii
1 INTRODUCTION .....	1
1.1 Background.....	1
1.2 Problem Description.....	2
2 LITERATURE REVIEW .....	6
3 OBJECTIVES.....	10
4 METHOD .....	11
4.1 Description of Facility.....	11
4.2 Test Setups.....	11
4.3 Model Geometry.....	13
4.3.1 Axisymmetric cavity.....	13
4.3.2 Two-dimensional cavity.....	14
4.4 Types of Test.....	14
4.4.1 Flow visualization.....	14
4.4.2 Digital particle image velocimetry (DPIV).....	17
4.4.3 Hotfilm measurement.....	19
5 RESULTS AND DISCUSSIONS.....	21
5.1 Dimensionless Parameters.....	21

5.2	Axisymmetric Cavity.....	22
5.2.1	Shaped-charge axisymmetric cavity .....	22
5.2.2	Straight axisymmetric cavities.....	28
5.2.2.1	Effect of aspect ratio .....	29
5.2.2.2	Effects of Reynolds number.....	37
5.2.2.3	Wake and upstream flow correlations.....	43
5.3	Two-Dimensional Cavity .....	44
5.3.1	Effect of aspect ratio .....	46
5.3.2	Effects of Reynolds number.....	53
6	CONCLUSIONS.....	59
	REFERENCES .....	62
	APPENDICES .....	66
	Appendix A: Effect of the bubble probes.....	67
	Appendix B: Flow visualizations .....	69
	Appendix C: Streamlines.....	75

## LIST OF FIGURES

Figure 1.1	PIM-77 air-dispersed grenade sub-munitions. ....	1
Figure 1.2	Grenade wind tunnel test time histories; damped (upper trace) and amplified (lower trace) oscillations. ....	2
Figure 1.3	Fluid dynamics instabilities: a) convective instabilities, b) absolute instabilities <sup>3</sup> .....	3
Figure 4.1	Axisymmetric cavity experimental setup.....	12
Figure 4.2	Two-dimensional cavity experimental setup. ....	12
Figure 4.3	a) Grenade model, b) axisymmetric cavity model, c) detail geometry of axisymmetric cavity model, AR = 1. ....	13
Figure 4.4	Detail geometry of two-dimensional cavity model, AR = 0.5.....	14
Figure 4.5	General setup for flow visualization. ....	15
Figure 4.6	a) Vertical bubble probe, b) Horizontal bubble probe. ....	16
Figure 4.7	PIV measurement setup. ....	17
Figure 4.8	Setup of hotfilm measurement. ....	20
Figure 5.1	Flow visualization of external flow at Re = 7000: a) trapped eddy, b) eddy ejection, c) merging of eddies with the wake.....	23
Figure 5.2	Flow structures inside the shaped-charge cavity at Re = 7000.....	24
Figure 5.3	Cartoon of cavity flow topology.....	25
Figure 5.4	Periodic fluid structures ejection, Re = 7000.....	26

Figure 5.5	Cavity fluid exchange/entrainment mechanism.....	28
Figure 5.6	Flow structures inside a straight cavity of AR = 1 at Re = 7000.....	29
Figure 5.7	Flow structures inside a straight cavity of AR = 2 at Re = 7000.....	30
Figure 5.8	Flow structures inside a straight cavity of AR = 0.5 at Re = 7000.....	30
Figure 5.9	a) Spectral content of the wake of a straight cavity of AR = 0.5, b) Strouhal number of various aspect ratios; Re = 7000.....	31
Figure 5.10	a) Nondimensionalized u-velocity contour map of AR = 1, b) Singular point locations of various aspect ratios; Re =7000. ....	32
Figure 5.11	Nondimensionalized geometric centerline u-velocity distribution of various aspect ratios at Re = 7000. ....	33
Figure 5.12	a) Vorticity contour inside a straight cavity of AR = 1, b) Maximum negative vorticity inside straight cavities of different aspect ratios; Re = 7000. ....	35
Figure 5.13	a) Vorticity contour of a straight cavity of AR = 1.5, b) Maximum negative vorticity of straight cavities with different aspect ratios; Re = 7000.....	36
Figure 5.14	Flow structures inside a straight cavity of AR = 1 at Re = 43000.....	37
Figure 5.15	Streamlines plot of a straight cavity of AR = 1 at Re = 43000.....	38
Figure 5.16	a) Nondimensionalized u-velocity contour map of AR = 1 and Re = 43000, b) Singular point locations of various aspect ratios at different Reynolds numbers.....	39
Figure 5.17	Nondimensionalized geometric centerline u-velocity distribution at various Reynolds numbers, AR = 1. ....	40

Figure 5.18	a) Vorticity contour of AR = 1.5 at Re = 26000, b) Maximum negative vorticity of straight cavities of various aspect ratios at different Reynolds numbers.....	41
Figure 5.19	a) Vorticity contour inside a straight cavity of AR = 1 at Re = 35000, b) Maximum negative vorticity inside straight cavities of various aspect ratios at different Reynolds numbers. ....	42
Figure 5.20	Spectral contents along stream wise directions (AR = 0.5 and Re = 11000): a) $x/d = 0$ , b) $x/d = 0.5$ , c) $x/d = 1$ , d) $x/d = 1.5$ .....	43
Figure 5.21	Flow visualization images of two-dimensional cavity: a) Vertical plane, b) Horizontal plane, c) Cross-sectional plane (viewed from 45° angle); AR = 0.5 and Re = 7000. ....	44
Figure 5.22	Cartoon of two-dimensional cavity topology: a) Top view, b) Front view.....	45
Figure 5.23	Flow visualization image of two-dimensional cavity of AR = 2 at Re = 7000.....	46
Figure 5.24	Streamline plots of the flowfield of two-dimensional forward facing cavity: a) AR = 0.5, b) AR = 2; Re =7000.....	47
Figure 5.25	a) Nondimensionalized u-velocity contour map of AR = 1, b) Singular point locations of various aspect ratios; Re =7000. ....	48
Figure 5.26	Nondimensionalized geometric centerline u-velocity distribution of various aspect ratios, Re = 7000. ....	49
Figure 5.27	a) Vorticity contour of AR = 1.5, b) Maximum negative vorticity as a function of aspect ratio; Re = 7000.....	50

Figure 5.28	The wake of two-dimensional forward facing cavity of AR = 0.5 at Re = 7000: a) Streamlines plot, b) Vorticity contour.....	51
Figure 5.29	a) Power spectrum density of AR = 0.5, b) Strouhal number variations as a function of aspect ratio; Re = 7000.....	52
Figure 5.30	Flow visualization image of two-dimensional forward facing cavity; AR = 0.5 and Re = 43000. ....	53
Figure 5.31	Streamline plots of the flowfield of two-dimensional forward facing cavity: a) Re = 26000, b) Re = 43000; AR = 1.....	54
Figure 5.32	a) Nondimensionalized u-velocity contour map of AR = 1 and Re = 26000, b) Singular point locations of various aspect ratios at various Reynolds numbers.....	55
Figure 5.33	Nondimensionalized geometric centerline u-velocity distribution at various Reynolds numbers, AR = 1.5. ....	56
Figure 5.34	a) Vorticity contour of AR = 0.5 and Re = 35000, b) Maximum negative vorticity as a function of Reynolds numbers at various aspect ratios.....	57
Figure 5.35	a) Power spectrum density of AR = 1 and Re = 43000, b) Strouhal number of various aspect ratios at various Reynolds numbers.....	58
Figure A. 1	Cavity flow mean velocity vector map; a) undisturbed, b) disturbed.....	68
Figure B. 1	Flow visualizations of axisymmetric cavity at Re = 7000: a) AR = 0.5, b) AR = 1, AR = 1.5, c) AR = 2.....	69
Figure B. 2	Flow visualizations of axisymmetric cavity at Re = 21000: a) AR = 0.5, b) AR = 1, AR = 1.5, c) AR = 2.....	70

Figure B. 3	Flow visualizations of axisymmetric cavity at $Re = 26000$ : a) $AR = 0.5$ , b) $AR = 1$ , $AR = 1.5$ , c) $AR = 2$ .....	70
Figure B. 4	Flow visualizations of axisymmetric cavity at $Re = 35000$ : a) $AR = 0.5$ , b) $AR = 1$ , $AR = 1.5$ , c) $AR = 2$ .....	71
Figure B. 5	Flow visualizations of axisymmetric cavity at $Re = 43000$ : a) $AR = 0.5$ , b) $AR = 1$ , $AR = 1.5$ , c) $AR = 2$ .....	71
Figure B. 6	Flow visualizations of two-dimensional cavity at $Re = 7000$ : a) $AR = 0.5$ , b) $AR = 1$ , $AR = 1.5$ , c) $AR = 2$ .....	72
Figure B. 7	Flow visualizations of two-dimensional cavity at $Re = 21000$ : a) $AR = 0.5$ , b) $AR = 1$ , $AR = 1.5$ , c) $AR = 2$ .....	72
Figure B. 8	Flow visualizations of two-dimensional cavity at $Re = 26000$ : a) $AR = 0.5$ , b) $AR = 1$ , $AR = 1.5$ , c) $AR = 2$ .....	73
Figure B. 9	Flow visualizations of two-dimensional cavity at $Re = 35000$ : a) $AR = 0.5$ , b) $AR = 1$ , $AR = 1.5$ , c) $AR = 2$ .....	73
Figure B. 10	Flow visualizations of two-dimensional cavity at $Re = 43000$ : a) $AR = 0.5$ , b) $AR = 1$ , $AR = 1.5$ , c) $AR = 2$ .....	74
Figure C. 1	Streamlines around the axisymmetric cavity at $Re = 7000$ : a) $AR = 0.5$ , b) $AR = 1$ , $AR = 1.5$ , c) $AR = 2$ .....	75
Figure C. 2	Streamlines around the axisymmetric cavity at $Re = 21000$ : a) $AR = 0.5$ , b) $AR = 1$ , $AR = 1.5$ , c) $AR = 2$ .....	76
Figure C. 3	Streamlines around the axisymmetric cavity at $Re = 26000$ : a) $AR = 0.5$ , b) $AR = 1$ , $AR = 1.5$ , c) $AR = 2$ .....	76

Figure C. 4	Streamlines around the axisymmetric cavity at $Re = 35000$ : a) $AR = 0.5$ , b) $AR = 1$ , $AR = 1.5$ , c) $AR = 2$ .....	77
Figure C. 5	Streamlines around the axisymmetric cavity at $Re = 43000$ : a) $AR = 0.5$ , b) $AR = 1$ , $AR = 1.5$ , c) $AR = 2$ .....	77
Figure C. 6	Streamlines around the two-dimensional cavity at $Re = 7000$ : a) $AR = 0.5$ , b) $AR = 1$ , $AR = 1.5$ , c) $AR = 2$ .....	78
Figure C. 7	Streamlines around the two-dimensional cavity at $Re = 21000$ : a) $AR = 0.5$ , b) $AR = 1$ , $AR = 1.5$ , c) $AR = 2$ .....	78
Figure C. 8	Streamlines around the two-dimensional cavity at $Re = 26000$ : a) $AR = 0.5$ , b) $AR = 1$ , $AR = 1.5$ , c) $AR = 2$ .....	79
Figure C. 9	Streamlines around the two-dimensional cavity at $Re = 35000$ : a) $AR = 0.5$ , b) $AR = 1$ , $AR = 1.5$ , c) $AR = 2$ .....	79
Figure C. 10	Streamlines around the two-dimensional cavity at $Re = 43000$ : a) $AR = 0.5$ , b) $AR = 1$ , $AR = 1.5$ , c) $AR = 2$ .....	80



## NOMENCLATURE

<u>Symbols</u>	<u>Description</u>
$AR$	Aspect Ratio
$D$	Model diameter (axisymmetric cavity)
$d$	Cavity diameter (axisymmetric cavity)
$f$	Frequency
$H$	Model height (two-dimensional cavity)
$h$	Cavity height (two-dimensional cavity)
$l$	Cavity length
$Re$	Reynolds number
$S_i$	The $i^{\text{th}}$ singular/saddle point
$St$	Strouhal number
$U_\infty$	Freestream velocity
$\vec{V}$	Velocity vector
$u, v, w$	Velocity component in x, y and z direction respectively
$x, y, z$	Right hand coordinate system
<u>Greek symbols</u>	
$\theta$	Angular displacement of the grenade in x-z plane
$\nu$	Kinematic viscosity

$$\xi \quad \text{Vorticity} = \frac{\partial v}{\partial x} - \frac{\partial u}{\partial y}, s^{-1}$$

### Subscripts

$$i \quad i = 1, 2, 3, \dots$$

$D$  Based on model diameter (axisymmetric cavity)

$H$  Based on height (two-dimensional cavity)

# 1 INTRODUCTION

## 1.1 Background

PIM-77 air-dispensed grenade submunitions (Figure 1.1) are ribbon stabilized, and designed to descend vertically and impact the target at low angles of attack at a terminal velocity with minimum oscillations. During a series of wind tunnel tests on a full-scale grenade model, with a ribbon of various shapes and occasionally combined with cones or caps, four distinct stability characteristics were observed; ranging from exponentially damped oscillations, partly damped small amplitude oscillations, highly amplified oscillations, and locking onto a different angular attitude with superimposed low amplitude oscillations<sup>1</sup>.

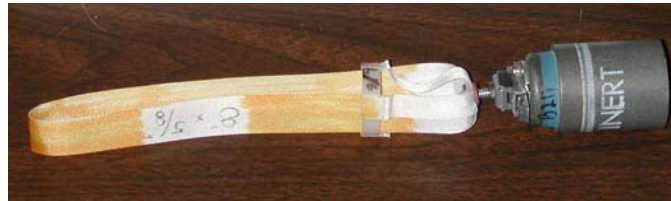


Figure 1.1 PIM-77 air-dispensed grenade sub-munitions.

The wind tunnel test setup consisted of a full scale grenade model with a built in 4-components balance to measure axial force, side force, yawing moment and pitching moment. In this setup, grenades were only allowed to oscillate in the horizontal plane. The yawing motion was measured by an angular displacement transducer. For every run, the grenade was locked at an initial angle and then released after the tunnel freestream

velocity reached the grenade terminal velocity. The Reynolds number range was 71000 to 117000<sup>1</sup>.

A post-launch time history of the grenade model deployed at 90 degrees to the direction of descent during the wind tunnel tests is shown in Figure 1.2. Since the model was constrained from oscillating in the vertical plane, oscillations represent yawing motion in the horizontal plane only<sup>1</sup>. In one case, the oscillations die quickly and the grenade approaches an equilibrium condition after release and in the second case oscillations continue to amplify after the grenade locks onto a different mode altogether. Figure 1.2 also shows that some ribbons were successful in damping the oscillations, while others contributed to instability introduced by fluid-structure interactions.

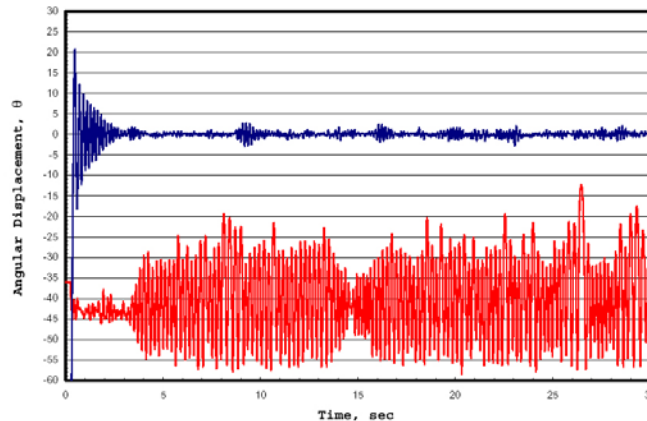


Figure 1.2 Grenade wind tunnel test time histories; damped (upper trace) and amplified (lower trace) oscillations.

## 1.2 Problem Description

From the time histories, it was evident that the flow in the wake of the grenade model was very complex and consisted of fluid-structures and fluid dynamics interaction of different kinds and magnitudes. These included the lock-in phenomena where resonance

is induced in the structure as the frequency of the flow fluctuation, or one of the harmonics, match the natural frequencies of the structure<sup>2</sup>. When resonance is induced in the structure, more flow fluctuation energy is absorbed by the structure and as a result the structure oscillates at the resonance frequency. In the case of a PIM-77 grenade, the unsteady wake structures shed asymmetrically from the grenade body with a certain periodicity. Periodic asymmetrical shedding caused fluctuations of aerodynamic forces acting on the grenade and the ribbon, and the frequency of these fluctuations was that of the wake shedding frequency. When the fluctuations frequency or one of the harmonics matched the natural frequency of the grenade or the ribbon, the ribbon stabilized grenade oscillated at that particular frequency. These oscillations either continued or amplified, as observed during the wind tunnel test. However, this relationship was not very clear. Additionally, the shedding of coherent structures in the wake has intrinsic instability features.

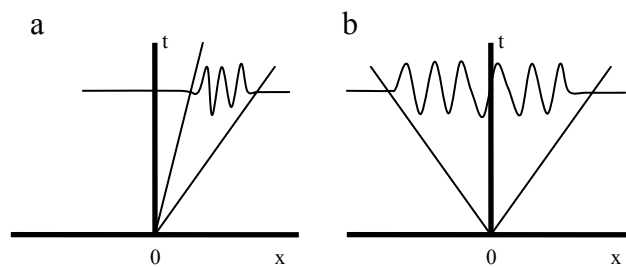


Figure 1.3 Fluid dynamics instabilities: a) convective instabilities, b) absolute instabilities<sup>3</sup>.

The fluid dynamic instabilities can be categorized into convective or absolute. In convective instability (Figure 1.3a), disturbances move away from the source and eventually leave the systems in their undisturbed states. Examples of convective instability are that of mixing layers and flat-plate wakes<sup>3</sup>. In the case of absolute

instability, as shown in Figure 1.3b, disturbances spread in both upstream and downstream directions, and gradually contaminate every spatial location in the flow field. Examples of absolute instability are that of hot or low density jets and bluff body wakes<sup>3</sup>.

PIM-77 grenades are axisymmetric bluff bodies with abrupt leading and trailing edges, whose shaped-charge geometry yields a unique feature resembling a forward facing cavity. Based on fluid dynamic instability categorization it is reasonable to assume that the shedding of the wakes of the grenade induces fluctuations on the flow inside the cavity which possibly result in additional oscillations of the grenades. In classic bluff bodies such as cylinders and spheres, the effects of wake shedding on the upstream flow are indicated by their strong correlations with forward singular point fluctuations.

For a bluff body, the singular point or attachment point also known as stagnation point is well established. By definition, the singular point is any point within the flow where the velocity of the flow is equal to zero<sup>4</sup>. For a potential flow, singular points appear in two locations on a bluff body, the leading edge and the trailing edge. In a real flow, due to viscous effects, more than one singular point may exist on the body with the primary one located near the leading edge of the body. Depending on the leading edge shape, this forward singular point is either attached to the body or located at a minuscule distance upstream. Studies have shown correlation between bluff body wakes and forward singular point fluctuations. Smith<sup>5</sup> studied forward singular point fluctuations of a circular cylinder and showed that the forward singular point fluctuations originated from unsteadiness of the wake. He pointed out the correlations between forward singular point fluctuations and wake shedding, and described the manner they affect each other. For a

circular cylinder, he also showed that the forward singular point fluctuated at the wake shedding frequency. Similar studies on the nature of the forward singular point of bluff bodies were done by Piercy and Richardson<sup>6</sup>, and Kuethe, et al.<sup>7</sup>. A study by Higuchi, et al.<sup>8</sup>, as will be discussed in more detail later, revealed the existence of a detached singular point inside a forward facing cavity. In contrast with the singular point of a classic bluff body whose nature and behavior are known and well defined, the nature and behavior of detached singular point are not well documented.

## 2 LITERATURE REVIEW

Bluff bodies, such as cylinders and spheres, have been a subject of numerous analytical, numerical and experimental studies. On the contrary, for a forward facing cavity, only limited information can be found in the literature. In 1968, Bastianon<sup>9</sup> numerically studied axisymmetric supersonic inviscid flow over a nonporous cavity and calculated the pressure fluctuation inside the cavity, and also explained the streamlines variation for a complete cycle of pressure fluctuations. He showed that the cycle starts with streamlines flowing smoothly over the interior of the cavity, and a uniform cavity pressure distribution. As the flow establishes, the cavity pressure starts to rise and a pressure peak develops near the internal corner of the cavity. At this stage, all gas particles approaching the pressure peak tend to slow down. If a particle has enough kinetic energy to overcome adverse pressure gradient due to cavity pressure build up, it continues to move along the cavity wall and exits the cavity. On the other hand, if a particle does not have sufficient kinetic energy to overcome the adverse pressure gradient, it stops, reverses its direction, and initiates the formation of a vortex type flow inside the cavity. The size of this vortex increases with time as more fluid particles accumulate within the cavity. When vortex becomes large enough, it sheds from the cavity and is carried away by the external flow. Afterward, as the pressure decreases and the kinetic energy of the approaching particles overcomes the adverse pressure gradient, initial condition for the beginning of a new cycle is reestablished. Dorrepaal, et al.<sup>10</sup>



analytically showed the formation of vortical structures in a forward facing cavity and also showed that for a spherical cap submerged in axisymmetric stokes flow, there is a ring vortex attached to cavity concave surface and the formation of this ring vortex is independent of the direction of the oncoming flow.

An aerodynamic decelerator, such as a parachute canopy, is the most common application of a forward facing cavity in the subsonic flow regime. Higuchi and Takahashi<sup>11</sup> conducted an experimental study on two-dimensional canopies. They focused their investigations on the aerodynamic characteristics of two-dimensional slotted bluff bodies using a series of thin flat plate arranged to form flat and curved geometries. They studied the effect of spacing ratio, curvature, and vent on the wake structures. They reported that, as the model curvature increased, the shedding frequency decreased. Consequently, the wakes became narrower and their motion was reduced. Hence, larger curvatures resulted in more stable and symmetric near-wake patterns. Additionally they discussed the effects of spacing ratio and vent on shedding of the vortices, stability of the wake structures and also the wake patterns. A flow visualization study by Higuchi<sup>12</sup> on the behavior of the wake behind solid and slotted axisymmetric bodies of a disk and parachute canopy shapes revealed intricate wake structures. Here he observed the wake oscillations for all configurations and noticed that the oscillations had lesser amplitudes for slotted bodies. He also reported that, for the slotted bodies, the recirculation zone was detached from the body. Further studies by Higuchi, et al.<sup>8</sup> on forward facing cavity were focused on the flow characteristic within concave-nosed body. Based on flow visualizations, they were able to identify the turning flow near the cavity entrance due to the reversal in direction of the flow entering the cavity. Also from

PIV measurements they found that the forward stagnation point developed within the cavity.

A more recent experimental study on the parachute canopy was conducted by Johari and Desabrais<sup>13</sup>. Their work was focused on vortex shedding in the near wake region. They reported that shear layers emanating from inside the parachute canopy caused periodic formation and shedding of a symmetric vortex ring in the vicinity of the canopy skirt. They also found that the Strouhal number of this periodic vortex shedding,  $St = 0.55$ , to be much greater than rigid bluff bodies such as disk,  $St \approx 0.14$ , and spheres,  $St \approx 0.2$ . However, farther downstream from the canopy, vortex characteristics in canopy wake were similar to the one of rigid bluff body wake.

Another common application of a forward facing cavity configuration is to reduce severe heating and ablation at the nose tip of supersonic and hypersonic vehicles. Engblom, et al.<sup>14</sup> conducted experimental and numerical studies of forward facing cavity in hypersonic flow regime with focus on the correlation between cavity pressure oscillation and flowfield structures with cavity geometry and found that pressure oscillations inside the cavity had strong correlations with cavity length and were dominated by quarter-wave frequency of the cavity. They also observed that the magnitude of the oscillations increased with cavity depth. Additionally, they reported correlations between cavity length and flow structures of the reattachment region and showed that the size of this region was affected by the cavity length. They also showed relationships between the pressure, cavity length and variations of the reattachment point locations. Similar observations were made by Yüceil and Dolling<sup>15</sup>. They found that with

an increase in cavity depth, the resonance frequency decreased and amplitude of pressure fluctuation increased. Another type of correlation between the cavity length and flow structure was studied by Hubner and Utreja<sup>16</sup>. They showed that, for a nose-cavity configuration, the bow-shock oscillation frequency and amplitude were directly related to the cavity depth.

### **3 OBJECTIVES**

There is very limited information available in the literature that deals with flowfield interaction of forward facing cavities. The objectives of the present investigation therefore were to determine and understand the fluid dynamics of the flowfield of forward facing cavities, with emphasis on the understanding of fluid exchange/entrainment mechanism, flow structures, nature of the primary singular point, and flow topology for different cavity aspect ratios and Reynolds numbers. Investigation also included the flowfield of two-dimensional cavities.

## 4 METHOD

### 4.1 Description of Facility

All tests were conducted in the Aerospace Engineering 45 cm x 45 cm cross-section test section water tunnel capable of operating with close or open surface condition. The 2 m long transparent test section provided optical access for flow visualizations and PIV measurements. A frequency controller continuously varied the tunnel speed from 0 – 1.1 m/s with the free stream turbulence intensity of < 1% at peak velocity.

### 4.2 Test Setups

Considering the limitation of maximum flow speed, the maximum Reynolds number chosen for water tunnel work was 43000. Five additional Reynolds numbers; 7000, 11000, 21000, 26000, 35000, were selected to provide the widest possible range for analysis. Since all tests performed in the water tunnel were under an open surface operation, the models were position in a vertical location where the effects of free surface were negligible. This location was approximately in the middle of the test section.

Figure 4.1 shows the experimental setup for the axisymmetric cavity. The model was mounted from the rear on a straight tube. The tube was connected to a C-strut, which is part of a specially built traversing mechanism rested on top of the tunnel sidewalls. The tube was connected to a gravity assisted dye injection system for flow visualization and

PIV seeding purposes. The center of the cavity entrance was chosen as the origin of the right hand coordinate system.

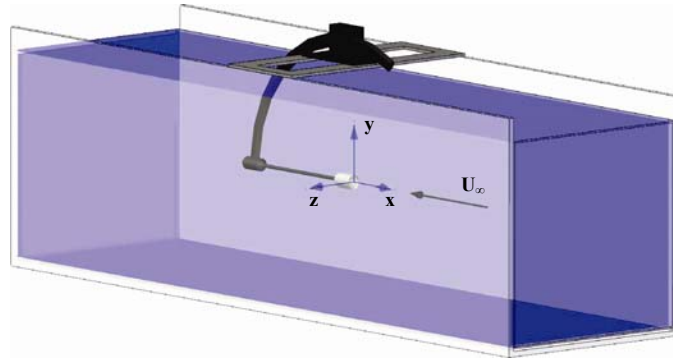


Figure 4.1 Axisymmetric cavity experimental setup.

The experimental setup for the two-dimensional cavity is shown in Figure 4.2. For rigid mounting purposes, the model was supported by four metal rods connected by metal plate attached to the top of the tunnel sidewalls. The supporting rods were positioned very close to the tunnel sidewalls so that their effect on the observation plane could be neglected.

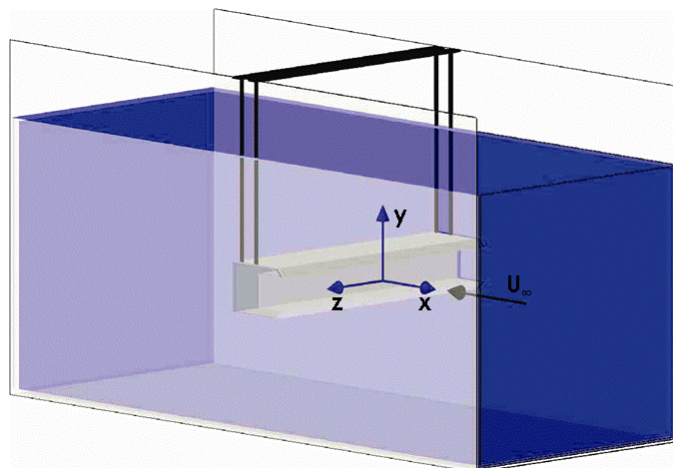


Figure 4.2 Two-dimensional cavity experimental setup.

## 4.3 Model Geometry

### 4.3.1 Axisymmetric cavity

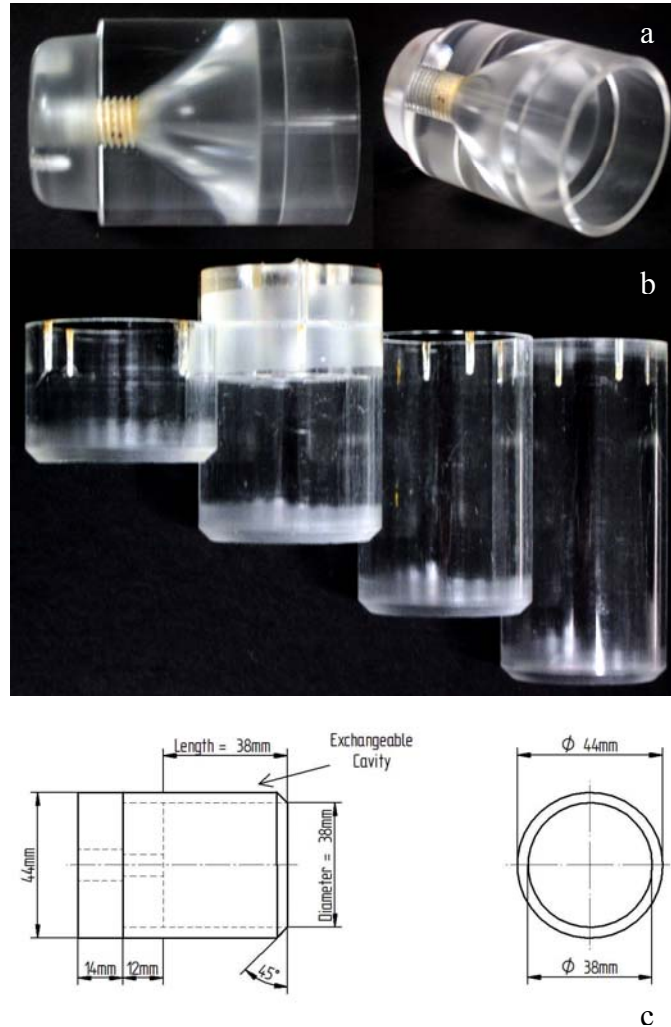


Figure 4.3 a) Grenade model, b) axisymmetric cavity model, c) detail geometry of axisymmetric cavity model, AR = 1.

Two types of axisymmetric cavity models were used in these investigations. The first was a full scale grenade model with a shaped-charge cavity configuration (Figure 4.3a). The second consisted of a solid round base and a set of tube forming a straight cavity of various lengths (Figure 4.3b). This length variation was to achieve cavity aspect ratio of 0.5, 1, 1.5 and 2, where cavity aspect ratio is defined as cavity length to diameter ratio.

All models were made of transparent acrylic and polished to provide access for observing phenomenon inside the cavity during the flow visualization and PIV. Figure 4.3c shows detail geometry of the second model for an aspect ratio of 1. A detailed description of the grenade can be found elsewhere<sup>1</sup>.

### 4.3.2 Two-dimensional cavity

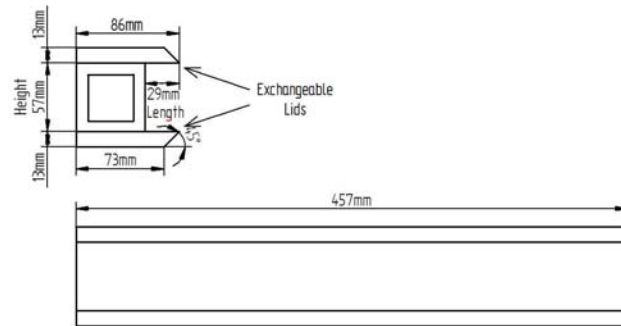


Figure 4.4 Detail geometry of two-dimensional cavity model, AR = 0.5.

The two-dimensional cavity model was made of a transparent acrylic sheet. The model was provided with exchangeable lids to provide cavity aspect ratio of 0.5, 1, 1.5 and 2, where, for the two dimensional cavity, aspect ratio is defined as cavity length to height ratio. Detail geometry for the two-dimensional cavity with aspect ratio of 0.5 is shown in Figure 4.4.

## 4.4 Types of Test

### 4.4.1 Flow visualization

Two flow visualization techniques employed in this work consisted of hydrogen bubbles and Planar Laser Induced Fluorescence (PLIF) of fluorescent dye. In some cases both techniques were used simultaneously. A typical setup for the flow visualization is



shown in Figure 4.5. The planes of observation were illuminated with laser light sheet generated by a combination of OZ Optics light sheet generator and 5W continuous wave front Argon Ion laser passing through fiber optic cable and a coupler also made by OZ Optics. The laser has a wavelength of 514.5 nm and hence it emits a visible green laser. The flow patterns were either recorded as standard video using a Cohu CCD camera and a JVC BR-S622DXU professional video recorder/player, or captured as sequence of images at 60 fps using Redlake Imaging Motionscope PCI-2000 high speed imager. These images were later post processed by using LabView Vision Assistant to further enhance flow features. A Sony thermal video printer was used to print selected images.

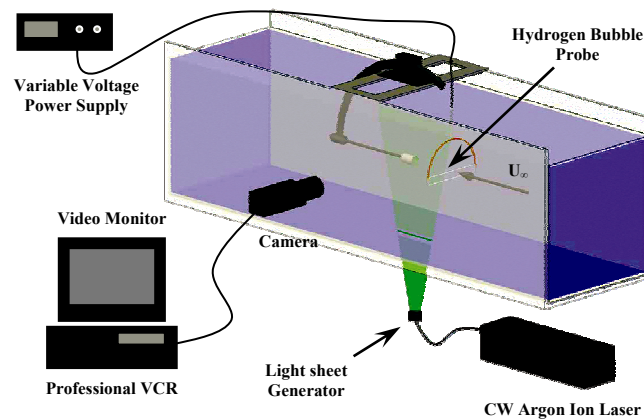


Figure 4.5 General setup for flow visualization.

For hydrogen bubble flow visualization, two types of probe were used. They were a single vertical wire probe (Figure 4.6a) and an equally spaced multiple horizontal wires probe (Figure 4.6b). Both probes were made using 32 Swg platinum wire. These probes were mounted on a two-degrees of freedom traversing mechanism for precise positioning. Bubbles were generated by applying a voltage across the bubble wire and a submerged stainless steel anode<sup>17</sup>. As these bubbles passed the laser illuminated the observation

plane, they scattered the light and made the flow patterns visible to the camera. The size and the quantity of the bubbles were controlled by adjusting the voltage, supplied from 3 power supplies connected in series, between 20 – 60 volts.

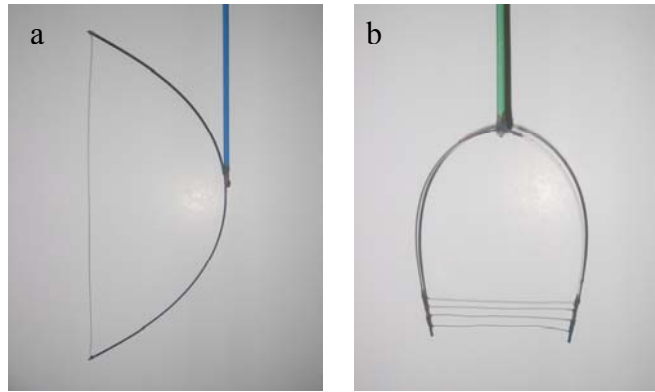


Figure 4.6 a) Vertical bubble probe, b) Horizontal bubble probe.

For PLIF, a solution of sodium fluorescein salt was stored in a dye reservoir located on the top of the tunnel. The solution was injected directly inside the cavity through the model support tube described earlier. Fluorescein has a bandwidth of absorbance that can be reached by an Argon ion laser<sup>17</sup>. Hence, as the entrained fluorescein solution passed through the laser light sheet, photons from the laser excited atoms of the fluorescein and made these atoms unstable. The excited atom dissipated the energy through intermolecular collisions which resulted in the emission of photon with bandwidth of wavelengths that included visible green light wavelength. As the result, the entrained fluorescein solution emitted green light and made the flow patterns visible.

#### 4.4.2 Digital particle image velocimetry (DPIV)

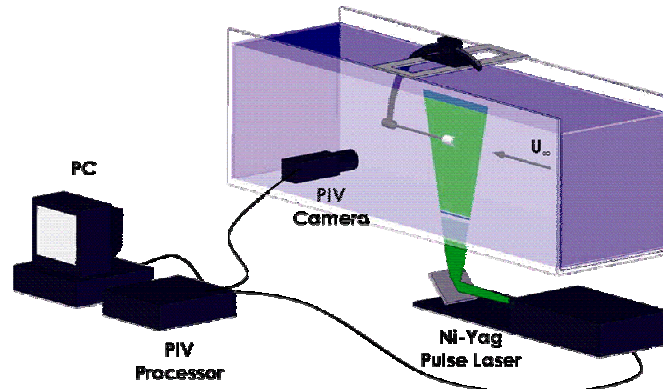


Figure 4.7 PIV measurement setup.

Figure 4.7 shows general setup for the PIV measurements. A Dantec Dynamics FlowMap PIV system, consisting of a NewWave Research 50 mJ dual pulse Nd:YAG laser, a Highsense 1k x 1k cross-correlation CCD camera and a PIV-2100 processor, was used to collect images that were processed using FlowManager software. Seeding particles used for PIV measurement were silver coated hollow glass spheres with an average diameter of 20  $\mu\text{m}$ . Time between two-consecutive laser pulses, for each measurement, was adjusted according to the speed of the flow. For measurements of the wake of the two-dimensional cavities, PIV measurements were phase averaged at the shedding frequency of the wake by incorporating TSI Constant Temperature Anemometry (CTA) system and pulse generator in the PIV system triggering mechanism. Flow statistics were computed from average of 1000 pairs of images. The area of interrogation used for cross-correlation computation was 32x32 pixels with 50% overlap. PIV data was later post processed with the help of Matlab and plotted with Tecplot.

DPIV is a computer aided non-intrusive quantitative flow visualization method. This method is based on the tracking of seeding particles displacements in the plane of observation illuminated by pulsed laser light sheets. By using this type of illumination, particles motions can be frozen for an instantaneous moment. Scattered lights from the illuminated particles during finite pulse duration of laser light are captured by a CCD camera, synchronized to the laser pulse rate and positioned perpendicular to the plane of observation, to form a series of images. Dual-pulse laser and a cross-correlation camera allow the system to significantly reduce images acquisition rate between a pair of consecutive images of the instantaneous particles locations in the illuminated observation plane. From a pair of sequential images, the magnitude and the direction of particles displacements is found. Since the camera is synchronized to the laser pulse, the time difference between two acquired images is equal to the time between two laser pulses. Hence based on the time and displacement information, the velocity of the particle is calculated.

An image can be treated as a two dimensional signal based on its intensity or the grey levels of the pixels. Hence in order to extract the particle displacement information from a pair of successive images, both images are subsampled with interrogation windows. These windows have a certain overlapping percentage with each other in order to reduce signal to noise ratio due to particles in an interrogation window of the first image has crossed the boundary of an interrogation window of the same location in the subsequent image. An average spatial shift of the particles within the two interrogation windows of the same location, with one being on the first image and the other one is on the subsequent image, may be observed through spatial cross-correlation. The cross-

correlation is carried out by taking an FFT of the sampled images, then performing a complex conjugate multiplication of each corresponding Fourier coefficients and finally taking the inverse FFT of the multiplications result. A peak in the cross-correlation result represents an average spatial shift of particles and its location can be found through Gaussian curve fitting. From this information and knowing the time between the two images as mentioned earlier, velocity vectors representing an averages displacement of particles from one interrogation window can be calculated. By doing the same processes for each interrogation windows; velocity vectors of the entire image can be obtained. From the velocity vectors, further analysis to calculate the streamlines, vorticity contour and etc. can be carried out.

#### **4.4.3 Hotfilm measurement**

In order to investigate the correlation between aspect ratio and the wake structures, hotfilm measurements were employed. Unlike DPIV, this technique is based on point measurements. The general experimental setup for this technique is shown in Figure 4.8, and consists of a TSI Inc. IFA-300 CTA system, an United Instrument data acquisition board and a TSI Inc 1260A-10W hotfilm probe. The probe was mounted on a Velmex Inc. traversing system for accurate positioning, and was located at  $x/D = 3$  downstream of the model trailing edge. A total of 1000 to 8000 samples were acquired at 50 and 100 Hz sampling rate, respectively, for each measurement. The data was later analyzed with Matlab signal processing routines. Additionally, the same setup was also used to determine the correlation between the wake and the upstream flow. This was

accomplished by taking measurements at different streamwise locations along the body of the models.

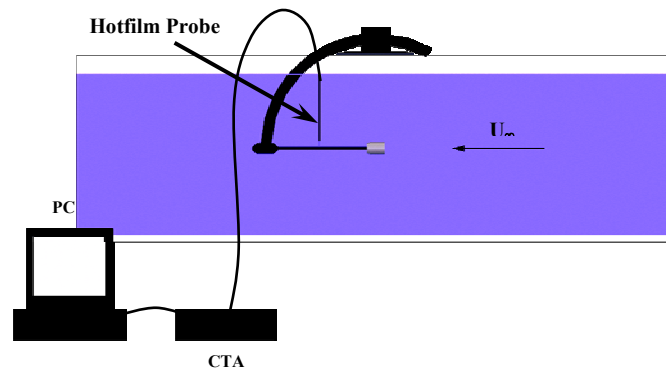


Figure 4.8 Setup of hotfilm measurement.

## 5 RESULTS AND DISCUSSIONS

Results of flow visualization using hydrogen bubbles and PLIF, and DPIV data were used to determine the characteristics of the flow. The DPIV results were analyzed to obtain quantitative explanations of the forward facing cavity flow phenomenon. Furthermore, time series analysis of hotfilm sensor signals was used to determine spectral contents of the flow.

### 5.1 Dimensionless Parameters

In describing these results, three dimensionless parameters; cavity aspect ratio, Reynolds number and Strouhal number, were used. As mentioned in the previous chapter, cavity aspect ratio was defined as cavity length to diameter ratio (Eq.5.1) for axisymmetric cavity, and as cavity length to height ratio (Eq.5.2) for two-dimensional cavity.

$$AR = \frac{l}{d} \quad (5.1)$$

and

$$AR = \frac{l}{h} \quad (5.2)$$

Model diameter,  $D$ , was used as the characteristic length for the calculation of Reynolds number for axisymmetric cavity i.e.  $Re_D = \frac{U_\infty D}{\nu}$ . Similarly for two-dimensional cavity, the Reynolds number was based on the model height,  $H$ ,  $Re_H = \frac{U_\infty H}{\nu}$ . The corresponding Strouhal numbers were therefore  $St_D = \frac{fD}{U_\infty}$  and  $St_H = \frac{fH}{U_\infty}$  respectively.

## 5.2 Axisymmetric Cavity

As mentioned earlier, there were two types of axisymmetric models used; a grenade model with shaped-charge cavity of aspect ratio of one and a straight cavity with aspect ratios of 0.5, 1, 1.5 and 2.

### 5.2.1 Shaped-charge axisymmetric cavity

Since only limited information on forward facing cavity flow is available in the literature, flow visualization tests were conducted not only to determine the feature of the flow but also to establish the desired test condition for the other tests. To visualize the flow inside the cavity, fluorescein solutions were directly injected into the cavity. When illuminated with an Argon ion laser, it was found that the entire flow within the cavity was not discernible, because fluorescein did not disperse uniformly in the cavity due to the presence of the flow structures whose existence was later confirmed by hydrogen bubbles technique. However, several important flow features were still observable.



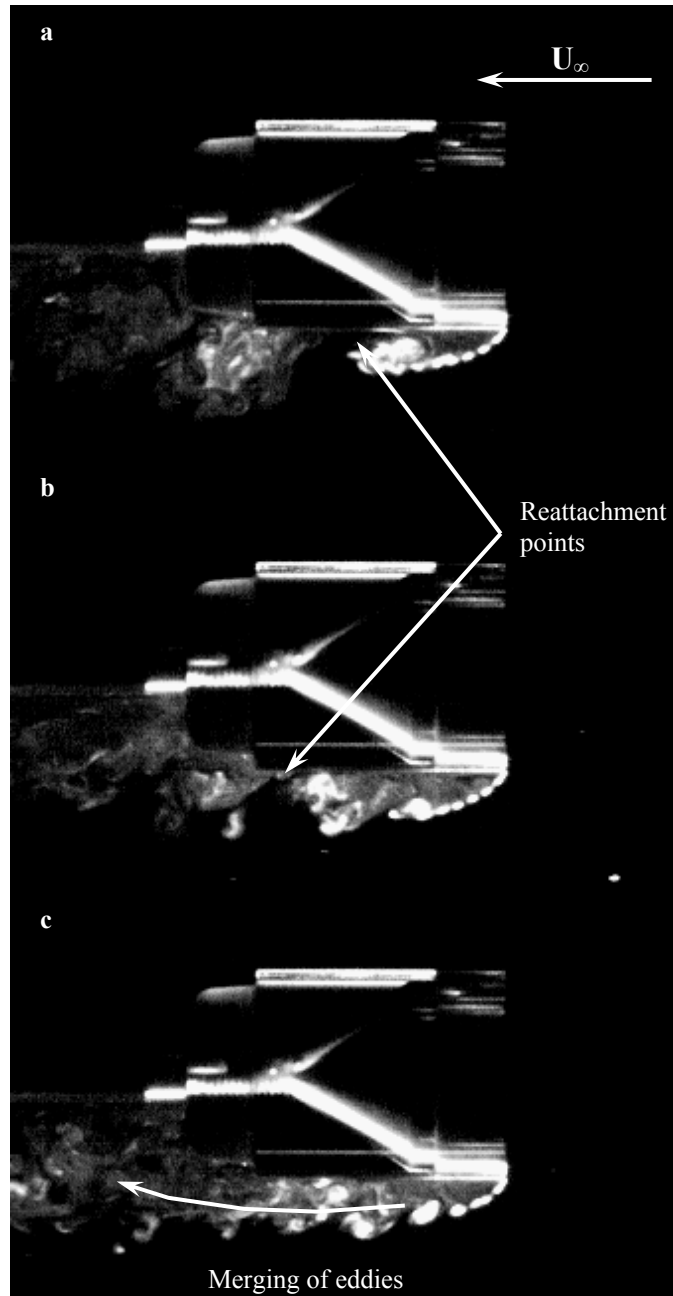


Figure 5.1 Flow visualization of external flow at  $Re = 7000$ : a) trapped eddy, b) eddy ejection, c) merging of eddies with the wake.

Figure 5.1 shows flow visualization results at Reynolds number of 7000. The important flow features shown in the figure are reattachment point oscillations due to wake instability, oscillations within the recirculating regions, periodic fluid structures ejection from inside the cavity and formation of shear layer vortices. Additionally, the

process of merging of eddy structures, emanating from the cavity, with the wake, as they convect downstream, is shown in Figure 5.1c.

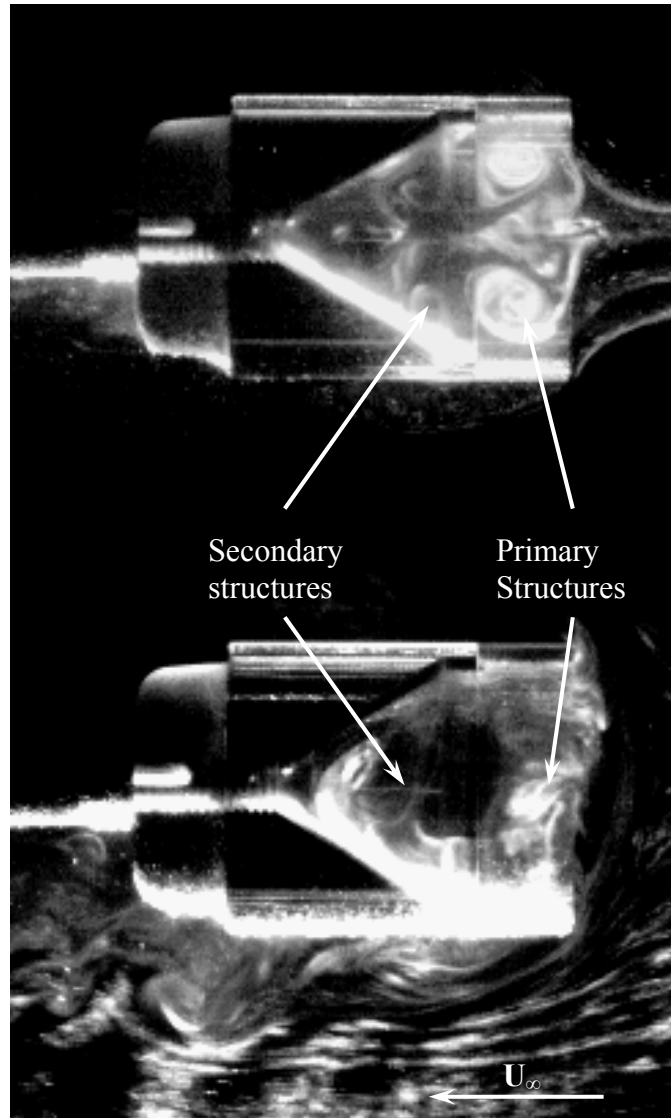


Figure 5.2 Flow structures inside the shaped-charge cavity at  $Re = 7000$ .

To visualize the entire flowfield, hydrogen bubbles were incorporated into the flow visualization tests. Thus for the same test conditions, the details of the cavity flow pattern became discernible, as shown in Figure 5.2. The top image corresponds to combination of PLIF and hydrogen bubbles generated by the equally spaced multiple horizontal wires

probe, and the bottom image shows the result of PLIF combined with single vertical wire probe. Figure 5.2 shows two vortical structures formed inside the cavity and these structures are referred to as primary and secondary structures, with the primary being the one closer to cavity entrance. Formation of vortical structures in forward facing cavity has been previously shown numerically and analytically<sup>9,10</sup>.

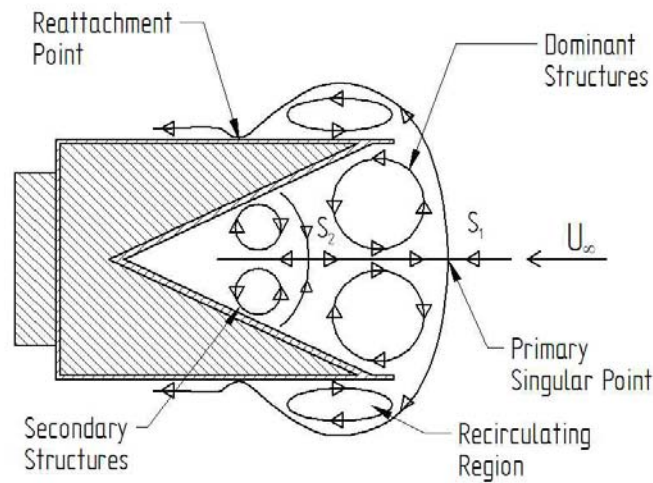


Figure 5.3 Cartoon of cavity flow topology.

It was observed that the existence of primary and secondary structures inside the cavity resulted in the formation of two singular points that were referred to as primary and secondary singular points. In Figure 5.2, the primary singular point is the one upstream; where the oncoming streamlines, marked by bubbles, bifurcate as they approach the cavity, and the secondary is the one downstream; in between the primary and secondary structures. Higuchi, et al.<sup>8</sup> also observed the development of singular point within a forward facing cavity. A topological model based on flow visualization results of the shaped-charge cavity is shown in Figure 5.3.

Analysis of flow visualization videos and a sequence of images captured with high speed camera revealed complex fluid dynamic interactions in the entire flow field. It was observed that both primary and secondary structures formed inside the cavity were spatially unstable and their formation was unsteady. Primary and secondary singular points also followed trends similar to the vortical structures and were observed to be oscillating. Additionally, after sufficient entrainment of outer flow, these flow structures were periodically ejected from the cavity. One such eddy structure is visible in Figure 5.4.

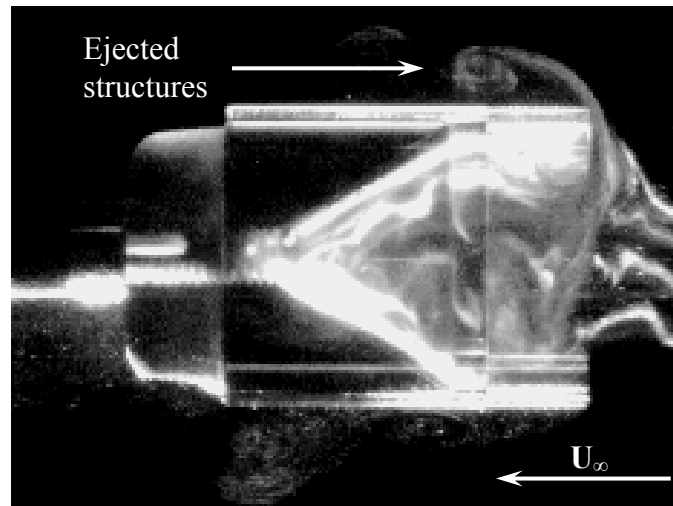


Figure 5.4 Periodic fluid structures ejection,  $Re = 7000$ .

Cartoons of one complete cycle of cavity fluid exchange/entrainment mechanisms are shown Figure 5.5 and their temporal evolution is described as follow. At the beginning of the cycle, fluid particles approaching the cavity experience adverse pressure gradient and reverse their direction before reaching the cavity base. This flow reversal results in the formation of the primary singular point,  $S_1$ , where the approaching streamline bifurcates

(Figure 5.5a). This is similar to the flow reversal phenomenon observed by Bastianon<sup>9</sup> and Higuchi, et al.<sup>8</sup> in a forward facing cavity.

As the bifurcating streamline traverses the entrance of the cavity, it sets in motion to counter rotating structures. With time progresses, secondary flow structures appear to satisfy the kinematics and establish the secondary singular point,  $S_2$  (Figure 5.5b). It was mentioned earlier that asymmetric vortex shedding behind a bluff body induced instability in both upstream and downstream of the body. Thus, in the case of a forward facing cavity, the asymmetric vortex shedding imposes an asymmetry in both primary and secondary structures with one being stronger and bigger than the other (Figure 5.5c).

Due to entrainment and interaction between these structures and the boundary layer on the side walls of cavity, the primary structures are asymmetrically squeezed and ejected out of the cavity. This results in the perturbation of the primary singular point. During the ejections process, the reattachment points are open, allowing the ejected structures to convect downstream and merge with the wake. Consequently, after the ejected structures coalesce with the wake flow, the oscillations continue as a new cycle.

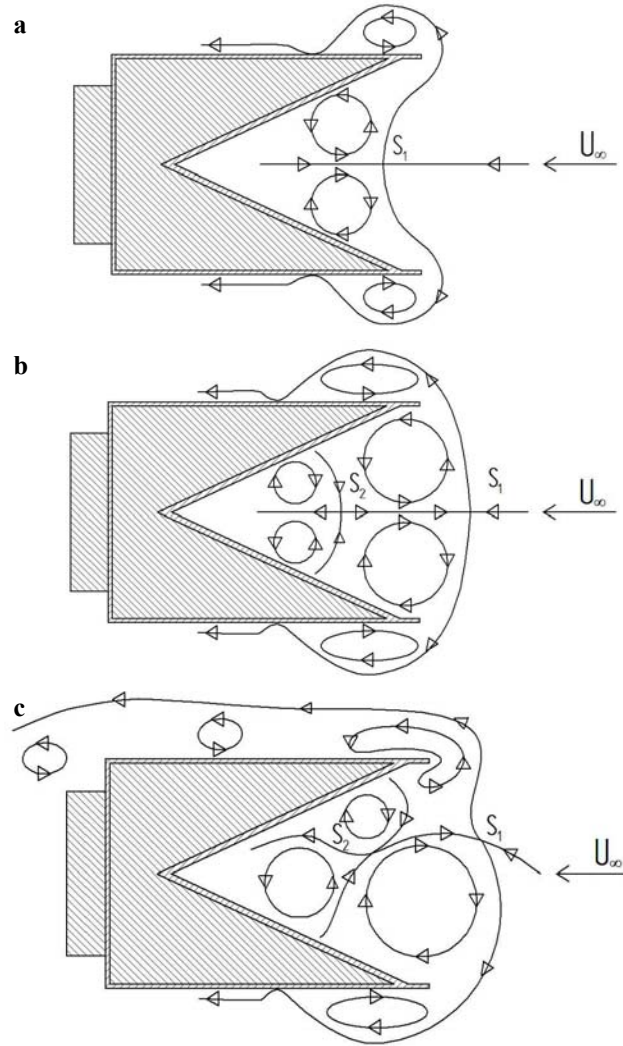


Figure 5.5 Cavity fluid exchange/entrainment mechanism.

### 5.2.2 Straight axisymmetric cavities

Previous studies have shown strong correlations between the aspect ratio of a forward facing cavity and the fluid dynamics<sup>14-16</sup>. Since a shaped-charge cavity of a PIM-77 grenade only yields an aspect ratio of one, straight cavity models with various aspect ratios were used to further investigate the correlations between cavity aspect ratio and fluid dynamics. Additionally, these models were also used to study Reynolds number effects on the flow of forward facing cavity of various aspect ratios.

### 5.2.2.1 Effect of aspect ratio

Flow visualization of a straight cavity of aspect ratio 1 revealed flow topology (Figure 5.6) and fluid exchange/entrainment mechanism similar to the one observed in the shaped-charge cavity case. This indicates that the kinematics of the flow inside a forward facing cavity was not sensitive to cavity shape. This, however, is not true for the forward facing cavity with bleed as observed by Higuchi, et al.<sup>8</sup>.

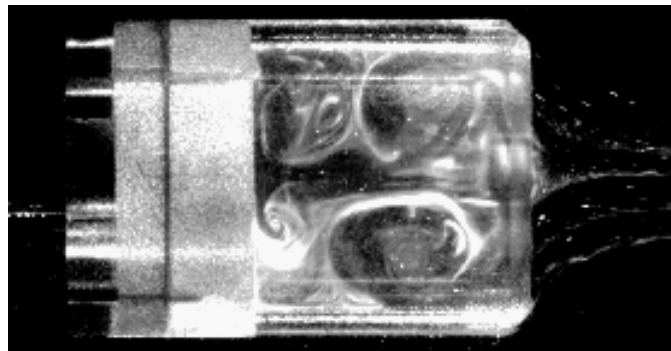


Figure 5.6 Flow structures inside a straight cavity of  $AR = 1$  at  $Re = 7000$ .

Analysis of video records showed that an increase in cavity aspect ratio led to more stretching of the primary structures and the formation of additional flow structures in the nearly stagnant region, near the back wall of the cavity, as shown in Figure 5.7. Interactions between these flow structures led to greater perturbations imposed on cavity flow, an increase in the instability of the vortical structures, and a subsequent rapid breakdown of the primary structures. Additionally, interaction between fluid structures and the stagnant region also resulted in sloshing motions of the stagnant region that contributed a certain level of instability to the fluid structures.

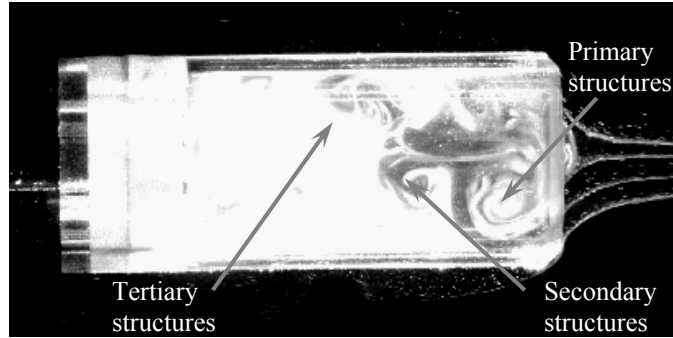


Figure 5.7 Flow structures inside a straight cavity of AR = 2 at Re = 7000.

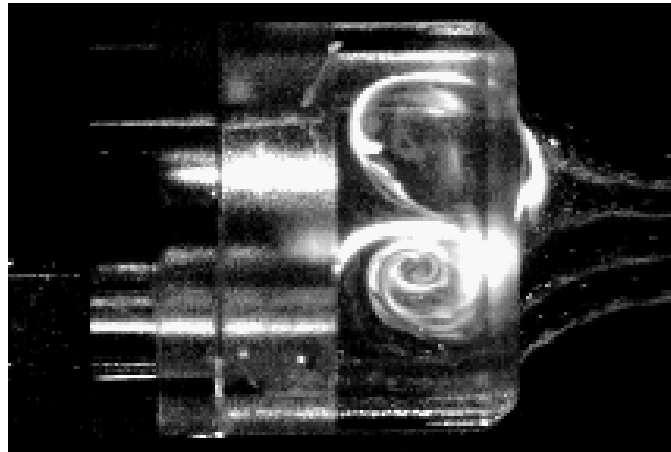


Figure 5.8 Flow structures inside a straight cavity of AR = 0.5 at Re = 7000.

It was also observed from flow visualization recordings that aspect ratio 0.5 had the most stable vortical structures (Figure 5.8). This was conjectured as due to the proximity of cavity base wall to the primary structures which resulted in the absence of the stagnant region and, consequently, more stable structures. This observation was also supported by the result of spectral analysis of the wake of axisymmetric forward facing cavities with different aspect ratios at Reynolds number of 7000 (Figure 5.9).



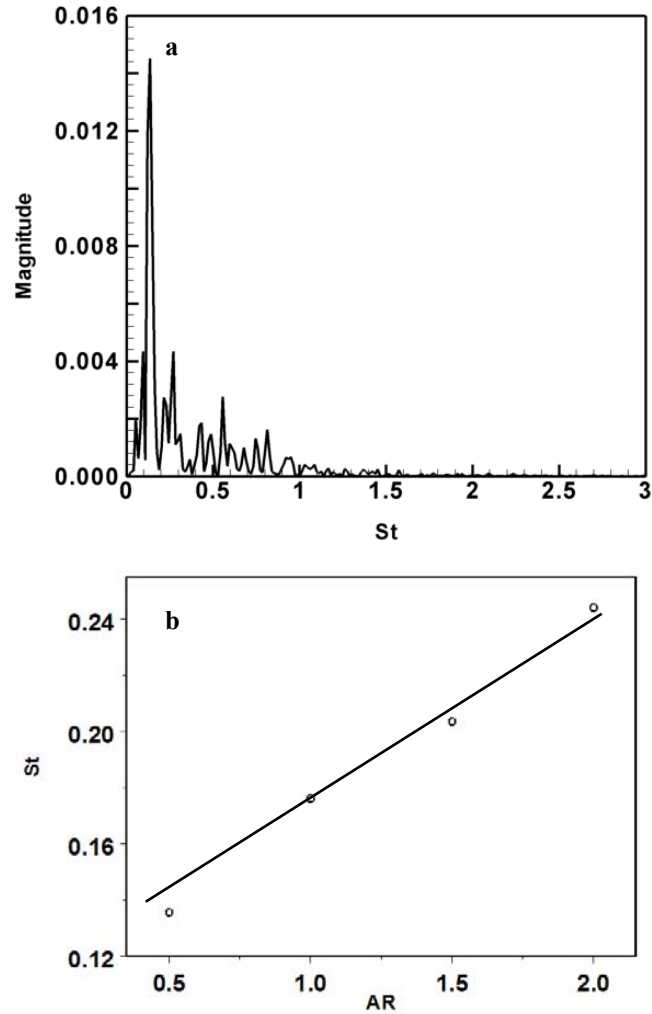


Figure 5.9 a) Spectral content of the wake of a straight cavity of AR = 0.5, b) Strouhal number of various aspect ratios; Re = 7000.

It is evident from Figure 5.9b that as the aspect ratio increases the Strouhal number of the wake also increases. Mentioned earlier that the wake of an axisymmetric forward facing cavity fell under absolute instability category, this implies that disturbances caused by the wake traveled in both upstream and downstream direction. Thus, increasing Strouhal number of the wake with aspect ratio implies that the instability imposed on the cavity structures also increased.

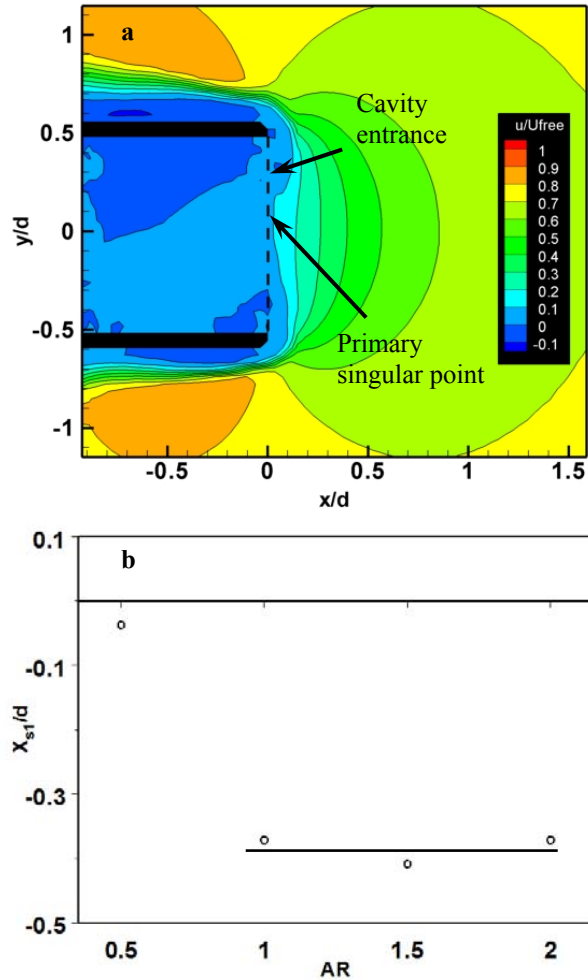


Figure 5.10 a) Nondimensionalized u-velocity contour map of AR = 1, b) Singular point locations of various aspect ratios; Re = 7000.

A region within the cavity entrance where the bifurcating streamline, due to the primary singular point, formed a stream surface was observed in the flow visualization recordings. This observation was corroborated by results of PIV measurements one of which is shown in Figure 5.10a as a contour plot of nondimensionalized mean u-velocity component. Results of the PIV measurements show that the mean location of singular point varies with a change in aspect ratio (Figure 5.10b). For low Reynolds number, Re = 7000, singular point location moves further downstream of the cavity as the aspect ratio

increases from 0.5 to 1 and remains almost unchanged for  $AR > 1$ . Similar observation was also made for the other Reynolds numbers used for this study.

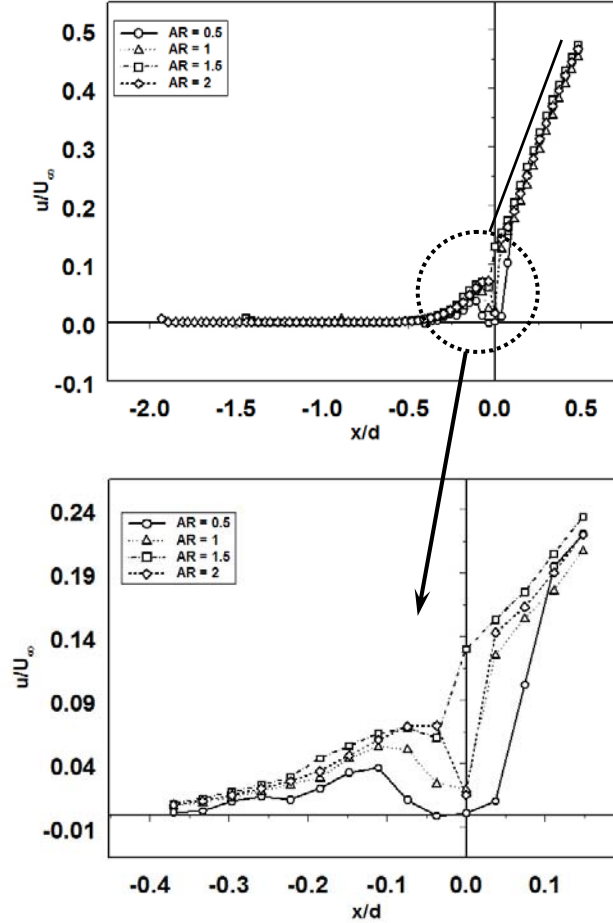


Figure 5.11 Nondimensionalized geometric centerline u-velocity distribution of various aspect ratios at  $Re = 7000$ .

The nondimensionalized geometric centerline mean u-velocity distribution extracted from PIV data of various aspect ratios for Reynolds number of 7000 is shown in Figure 5.11. It is evident from the figure that the velocity gradient of the oncoming flow at  $x/d > 0.1$  is not sensitive to changes in aspect ratio.

According to momentum equation (Eq.3.3), pressure gradient is related to velocity gradient.

$$\frac{\partial p}{\partial x} = -\rho u \frac{\partial u}{\partial x} \quad (5.3)$$

Thus, the velocity distribution shown in Figure 5.11 (top image) implies that, for  $x/d > 0.1$ , adverse pressure gradient due to deceleration of the oncoming flow did not depend on the cavity aspect ratio. However for  $x/d < 0.1$  the velocity distribution and, consequently, the pressure gradient show dependency on aspect ratio.

Figure 5.11 (bottom image) also shows that between  $0.05 < x/d < 0.1$  the velocity gradient, which also implies pressure gradient, decreases as the aspect ratio changes from 0.5 to 1 and remains constant for  $AR > 1$ . This also means that there was less pressure relaxations provided to the oncoming flow for aspect ratio 0.5. This phenomenon was due to the singular point location variations discussed earlier.

As shown in Figure 5.11, there is a local acceleration, which also implies a drop in pressure, indicated by emerging peak in the velocity distribution between  $-0.1 < x/d < 0$ . This local acceleration was due to streamlines curvature and the formation of fluid structures. Also shown in this figure is that the peak in the velocity distribution, due to local acceleration, increases as the aspect ratio increases. This was conjectured as due to the primary vortical structures inside the cavity became more stretched as the aspect ratio increased, as observed in the flow visualization recordings. Increasing velocity implies increasing vorticity and this result was corroborated by maximum negative vorticity data

calculated from PIV measurements shown in Figure 5.12b. Here, the negative sign indicates a clockwise rotation.

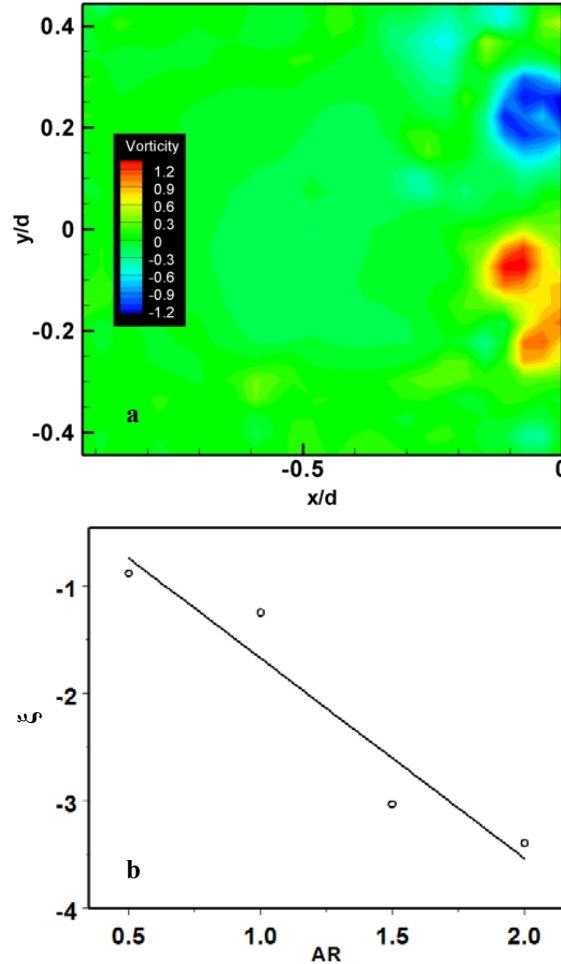


Figure 5.12 a) Vorticity contour inside a straight cavity of AR = 1, b) Maximum negative vorticity inside straight cavities of different aspect ratios; Re = 7000.

It is evident from Figure 5.12a that the vorticity of the cavity increases as the aspect ratio increases. Additionally, high vorticity results in more entrainment and mixing in the cavity flow, and Figure 5.12b implies an increase in large scale mixing within the cavity with increasing aspect ratio. This was also observed during the flow visualization tests and was indicated by more rapid breakdown of primary structures discussed earlier.

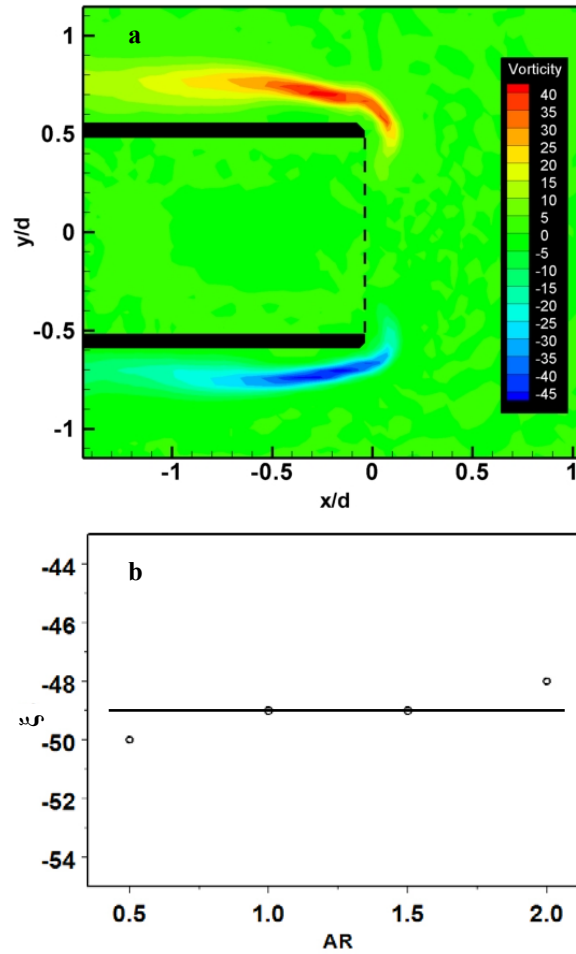


Figure 5.13 a) Vorticity contour of a straight cavity of  $AR = 1.5$ , b) Maximum negative vorticity of straight cavities with different aspect ratios;  $Re = 7000$ .

Vorticity of the whole flow field calculated from mean velocity, however, does not show a strong correlation with aspect ratio as shown in Figure 5.13b. Maximum negative vorticity which was found to be in the reattachment region (Figure 5.13a) remain almost constant with increasing aspect ratio. Positive maximum vorticity of both cavity and reattachment regions also exhibited similar behavior. Additionally, similar trend was also exhibited by maximum vorticity of both cavity and reattachment region, at all Reynolds numbers used in this study.

### 5.2.2.2 Effects of Reynolds number

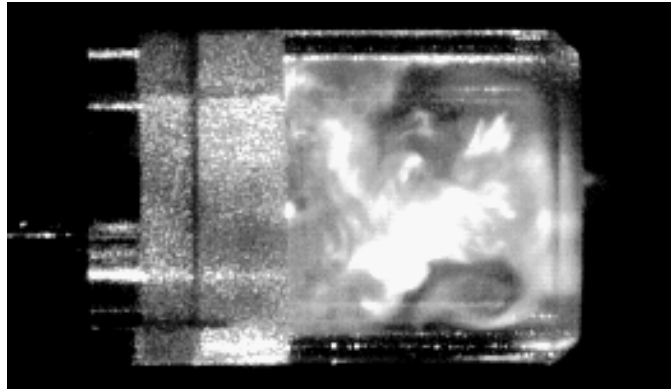


Figure 5.14 Flow structures inside a straight cavity of  $AR = 1$  at  $Re = 43000$ .

Effects of Reynolds number are discussed in this section. A flow visualization image, shown in Figure 5.14, shows flow structures similar to the one observed at lower Reynolds number. This indicates that kinematics of the cavity flow was not sensitive to changes in Reynolds number. However, it was observed from flow visualizations video that an increase in Reynolds number increased the unsteadiness of the flow structures inside the cavity. This was indicated by the cavity flow becoming more unsteady as the Reynolds number increased. Similar observations were also made from PIV measurement. Figure 5.15 shows streamlines calculated from average velocity data, and yields unstable cavity structures topology where one of the primary structures being more dominant and pushes its counter part out of the cavity. The ejected structures are indicated by a bulged area on the top body surface. Additionally, the bifurcating streamlines can also be observed from Figure 5.15.

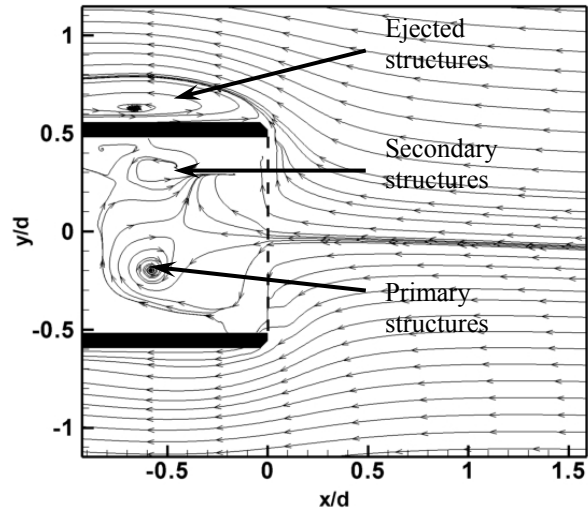


Figure 5.15 Streamlines plot of a straight cavity of  $AR = 1$  at  $Re = 43000$ .

Figure 5.16a shows a contour plot of nondimensionalized mean u-velocity component and a stream surface that yields the primary singular point for aspect ratio 1 at Reynolds of 43000. Data from PIV measurements, shown in Figure 5.16b, shows that the mean location of the singular point, which was found to be at  $x/d = -0.35$ , remains almost constant with an increase in Reynolds number. However, it is evident from the figure that singular point locations are slightly varied with aspect ratio. This result indicates that effects of aspect ratio on singular point locations were more dominant than Reynolds number.



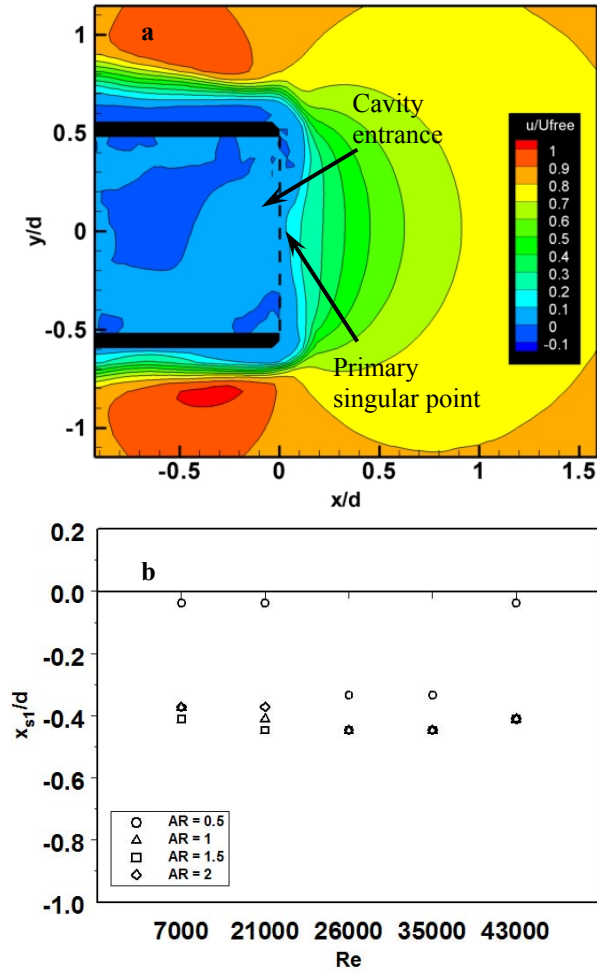


Figure 5.16 a) Nondimensionalized u-velocity contour map of AR = 1 and Re = 43000, b) Singular point locations of various aspect ratios at different Reynolds numbers.

Shown in Figure 5.17 is a nondimensionalized geometric centerline mean u-velocity distribution extracted from PIV data for aspect ratio 1 at various Reynolds numbers. It can be observed in the figure that as the Reynolds number increases the velocity gradient increases. This implies that the adverse pressure gradient increased with Reynolds number, and resulted in lesser pressure relaxation provided to the oncoming flow. Similar observation was also made for aspect ratio 0.5, 1.5 and 2.

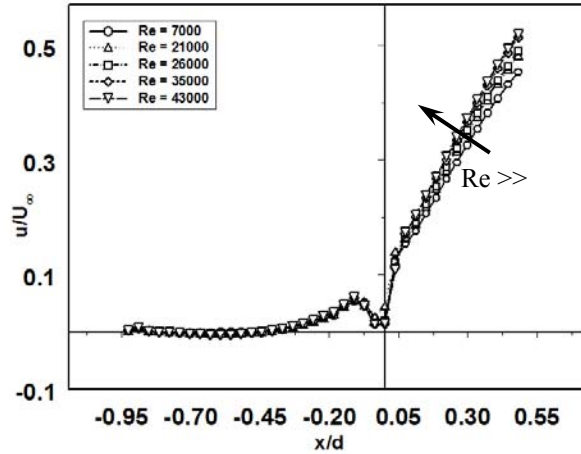


Figure 5.17 Nondimensionalized geometric centerline u-velocity distribution at various Reynolds numbers, AR = 1.

Effects of Reynolds number on reattachment region maximum negative vorticity for various aspect ratios are shown in Figure 5.18b. It is shown that vorticity increases as Reynolds number increases. Similarly with reattachment regions, vorticity inside the cavity tends to increase as the Reynolds number increases as shown in Figure 5.19b. Also shown in both Figure 5.18b and Figure 5.19b is that vorticity changes due to aspect ratio vary at different Reynolds numbers, and this implies that the effects of Reynolds number on vorticity were more dominant than aspect ratio. However, effect of aspect ratio is more pronounce on the vorticity of the cavity. Similar behaviors were also exhibited by maximum positive vorticity of both reattachment regions and cavity.

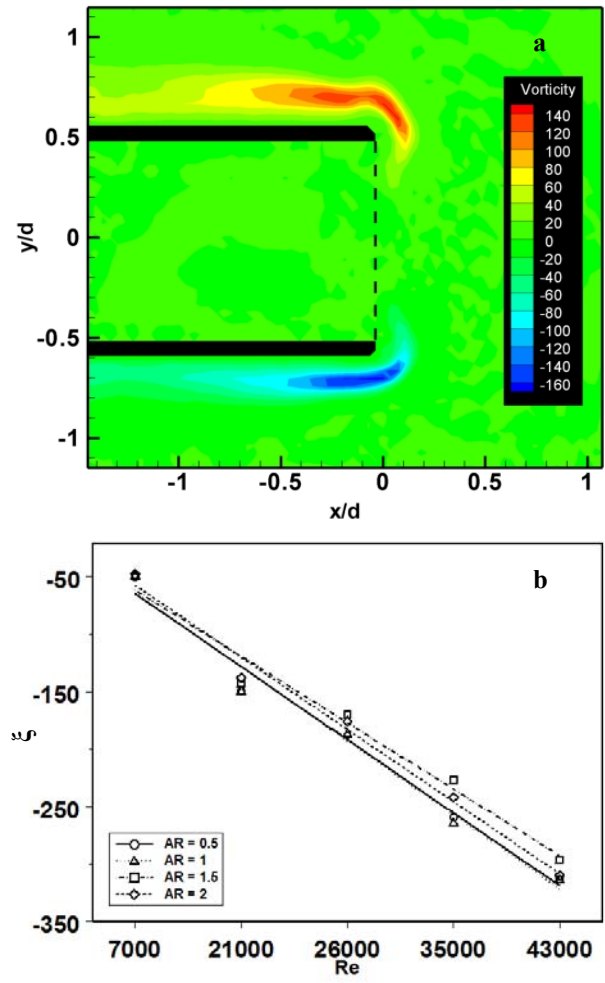


Figure 5.18 a) Vorticity contour of AR = 1.5 at Re = 26000, b) Maximum negative vorticity of straight cavities of various aspect ratios at different Reynolds numbers.

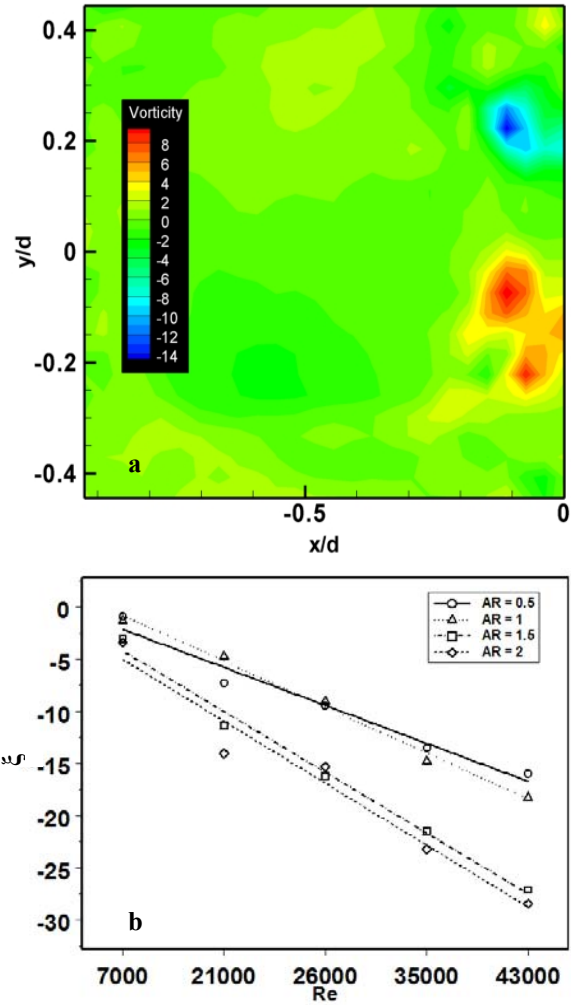


Figure 5.19 a) Vorticity contour inside a straight cavity of  $AR = 1$  at  $Re = 35000$ , b) Maximum negative vorticity inside straight cavities of various aspect ratios at different Reynolds numbers.

### 5.2.2.3 Wake and upstream flow correlations

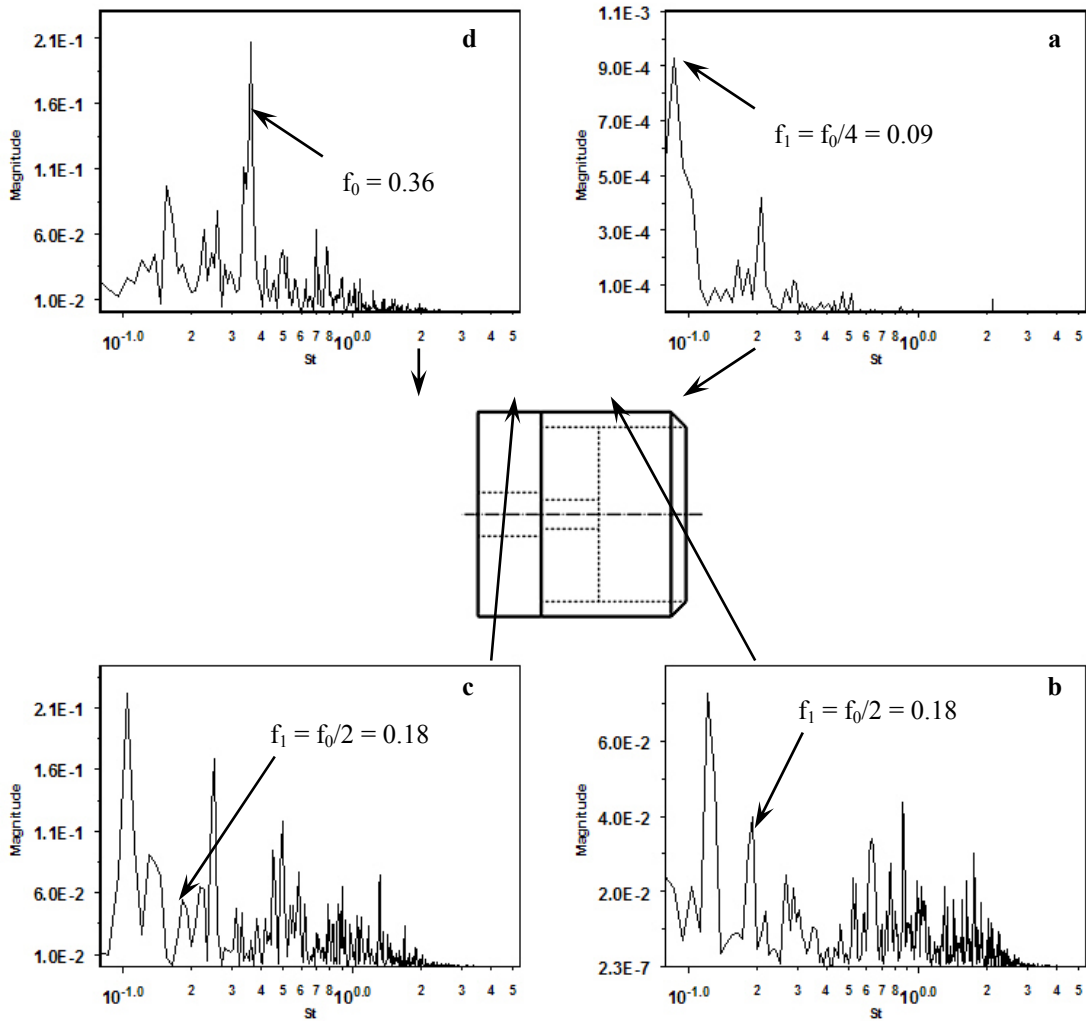


Figure 5.20 Spectral contents along stream wise directions ( $AR = 0.5$  and  $Re = 11000$ ): a)  $x/d = 0$ , b)  $x/d = 0.5$ , c)  $x/d = 1$ , d)  $x/d = 1.5$ .

As mentioned earlier, the instability due to the asymmetric shedding of the wake of a bluff body fell under the category of absolute instability, where the disturbances traveled in both upstream and downstream of the body. This means that there is a correlation between the wake and the upstream flow. In order to show this correlation several hotfilm measurements were taken at different streamwise locations along the body of the model,

and some of the results are shown in Figure 5.20. It can be observed from this figure that the magnitude of the disturbances is decreasing as the disturbances travel upstream of the wake region in the form of subharmonics disturbances. Figure 5.20a shows that frequency of the ejection of flow structures from inside the cavity is the subharmonics frequency of the shedding of the wake. This implies that asymmetric shedding of the wake imposed low frequency disturbances that resulted in asymmetric ejection of flow structures from inside the cavity.

### 5.3 Two-Dimensional Cavity

To further understand fluid dynamics of forward facing cavities, tests were extended to include two-dimensional forward facing cavity which is similar to two-dimensional inlets also known as Pitot inlets.

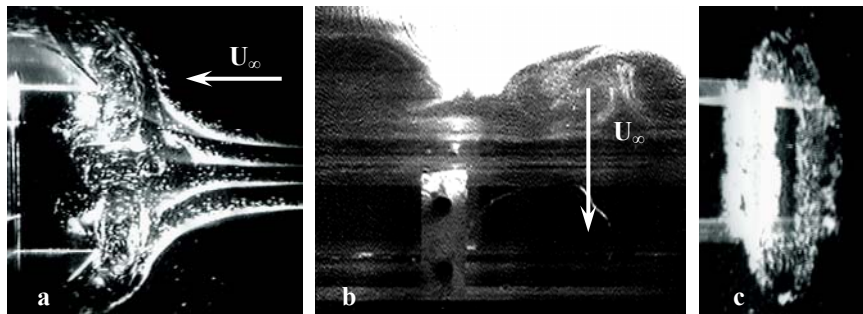


Figure 5.21 Flow visualization images of two-dimensional cavity: a) Vertical plane, b) Horizontal plane, c) Cross-sectional plane (viewed from  $45^\circ$  angle);  $AR = 0.5$  and  $Re = 7000$ .

Analysis of the flow visualization recordings revealed the formation of cellular vortical structures (Figure 5.21) and shear layer ejection which were observed to be the fluid exchange/entrainment mechanisms of the two-dimensional cavity. These mechanisms were observed to be periodic, and are described as follows. Initially,

oncoming streamlines bifurcated and, due to adverse pressure gradient, were forced to reverse their direction. This resulted in formation of vortical structures, which entrained more fluid particles and grew as time progressed.

Due to interactions between them and asymmetric shedding of the wake, these vortical structures became unstable and eventually broke down. Eddies that were part of these structures were entrained by the surrounding fluid, and this entrainment was immediately followed by shear layer emanating from the cavity. Similar to the case of axisymmetric cavity, reattachment points of the two-dimensional cavity were also open during the ejection period to allow the ejected structures to convect down stream and merged with the wake, and this process was then followed by the next cycle.

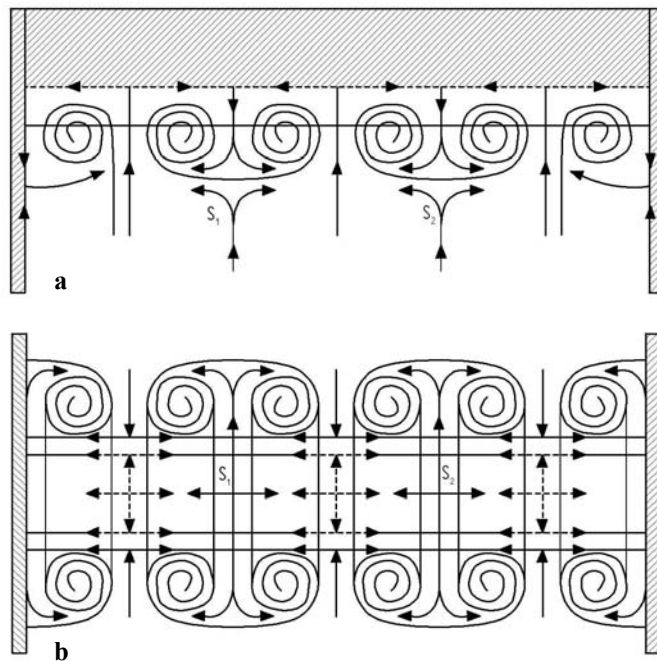


Figure 5.22 Cartoon of two-dimensional cavity topology: a) Top view, b) Front view.

A simple topology was made based on the flow visualization results and is shown in Figure 5.22. The topology consists of two end wall vortices and two cells of mushroom like vortical structures that are originating from inside the cavity and wrap around the top and bottom surfaces of the bluff body. Bifurcated oncoming streamlines in the spanwise direction result in two singular points,  $S_1$  and  $S_2$ .

### 5.3.1 Effect of aspect ratio

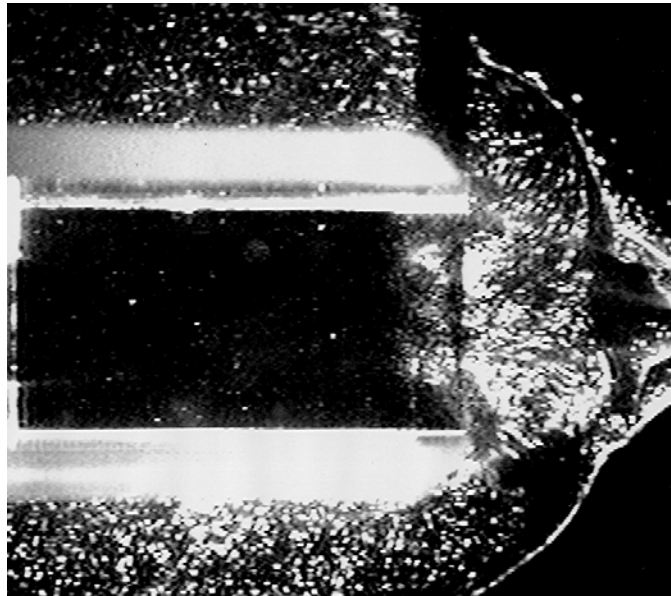


Figure 5.23 Flow visualization image of two-dimensional cavity of AR = 2 at  $Re = 7000$ .

Flow visualization of the two-dimensional cavities with various cavity aspect ratios revealed the formation of vortical structures and topology of the cavity flow that were similar to the one shown earlier (Figure 5.23). Unlike axisymmetric cavity, the number of structures formed inside the two-dimensional cavity was observed to be independent of cavity aspect ratio. Video analysis showed that cavity flow topology was preserved for all aspect ratios used in this work. This observation was confirmed by streamlines plots



calculated from PIV data two of which are shown in Figure 5.24. In this figure, the reversed streamlines indicate vortical structures location.

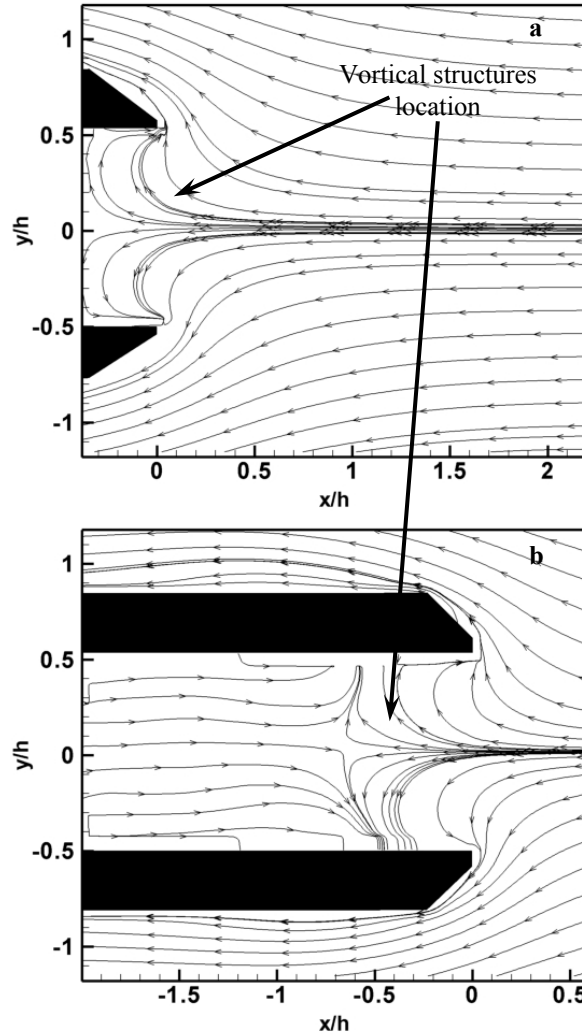


Figure 5.24 Streamline plots of the flowfield of two-dimensional forward facing cavity: a) AR = 0.5, b) AR = 2; Re = 7000.

Flow visualizations of the two-dimensional cavities also revealed that the stability of vortical structures was aspect ratio dependent, which is similar to the observations made for the axisymmetric cavity. It was observed that an increase in aspect ratio resulted in unstable vortical structures, and that aspect ratio 0.5 was observed to have the most stable

vortical structures. Similar to the axisymmetric cavity, this was again conjectured due to the presence of cavity base wall within cellular vortical structures proximity, which resulted in the absent of stagnant region and consequently more stable structures.

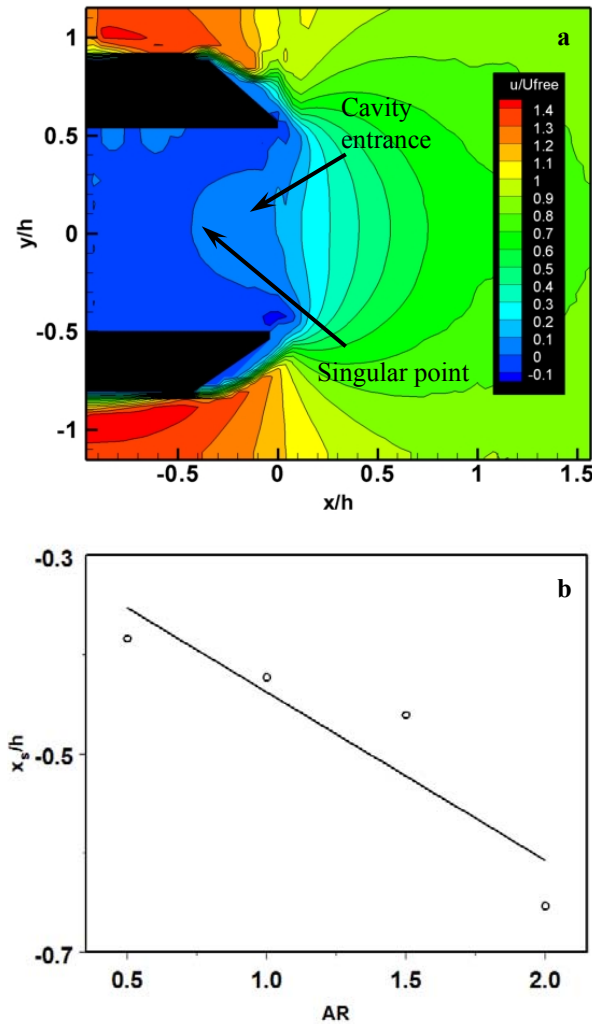


Figure 5.25 a) Nondimensionalized u-velocity contour map of AR = 1, b) Singular point locations of various aspect ratios; Re = 7000.

Stream surface, within the proximity of the cavity entrance, that yielded the singular point was also observed for two-dimensional cavity and shown in Figure 5.25a. PIV data

shows that for Reynolds number of 7000 the mean location of the singular point tends to move further downstream of the cavity with an increase in aspect ratio.

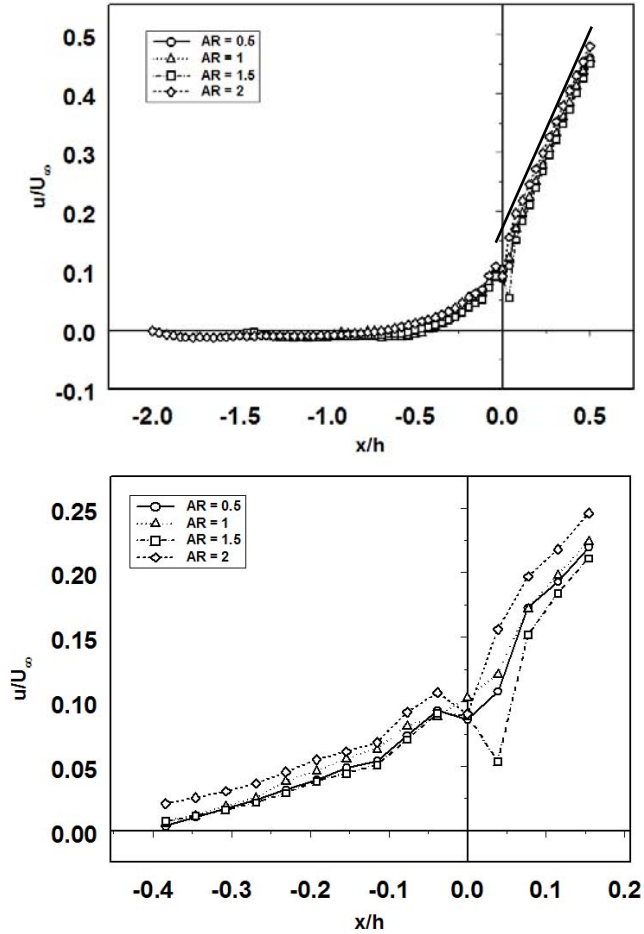


Figure 5.26 Nondimensionalized geometric centerline u-velocity distribution of various aspect ratios,  $Re = 7000$ .

Figure 5.26 shows the nondimensionalized geometric centerline mean u-velocity distribution of the two-dimensional cavity with various aspect ratios at Reynolds number of 7000. It can be observed from this figure that the velocity gradients for  $x/h > 0.15$  do not depend on the aspect ratio. Figure 5.26 also shows that for  $x/h < 0.15$  the velocity gradients vary with aspect ratio but do not show any particular trend. This result implies

that, for two-dimensional cavity, the velocity gradients and, consequently, the adverse pressure gradients were not sensitive to aspect ratio.

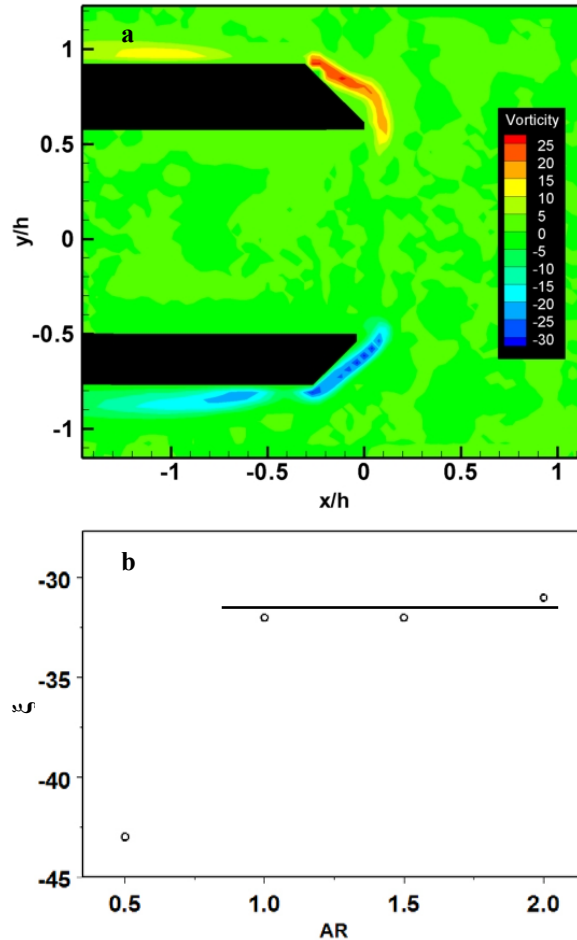


Figure 5.27 a) Vorticity contour of  $AR = 1.5$ , b) Maximum negative vorticity as a function of aspect ratio;  $Re = 7000$ .

It was shown earlier that, for axisymmetric cavities, vorticity of the reattachment region did not show a strong dependency on the aspect ratio. However, for the two-dimensional cavities, maximum negative vorticity of the reattachment region tend to decrease with increasing aspect ratio and approaches asymptotic value for  $AR > 1$ , as shown in Figure 5.27b. This implies that for two-dimensional cavity, vorticity of the reattachment region became insensitive to aspect ratio changes for  $AR > 1$ . Maximum

positive vorticity of the reattachment region followed a similar trend. For the two-dimensional cavity, insensitivity to changes in aspect ratio was also exhibited by cavity flow topology and velocity distribution along the centerline. Observations made for the other Reynolds numbers also indicated similar trend.

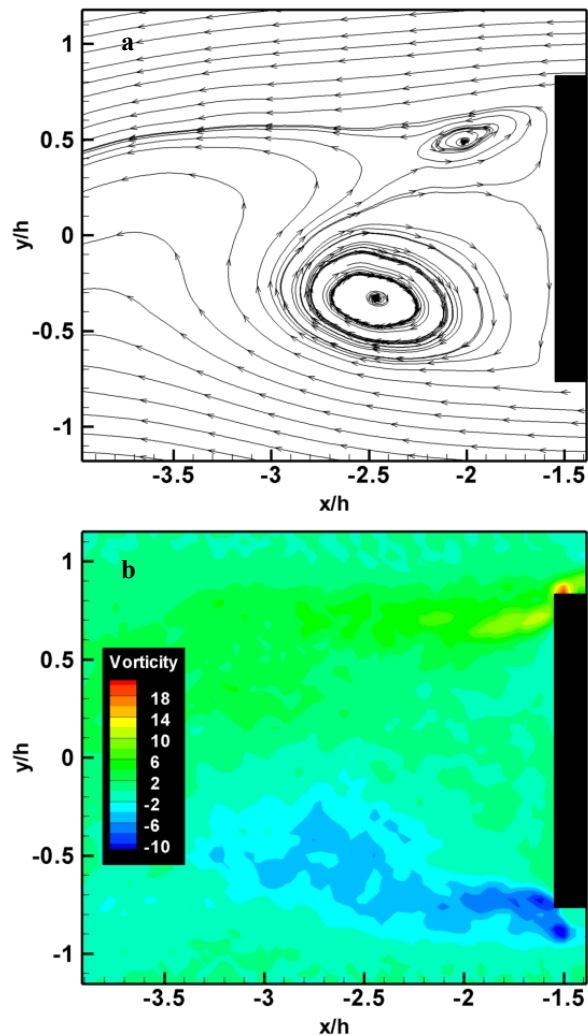


Figure 5.28 The wake of two-dimensional forward facing cavity of AR = 0.5 at  $Re = 7000$ : a) Streamlines plot, b) Vorticity contour.

Streamlines and a vorticity contour plot calculated from phase-averaged PIV measurements of the wakes of two-dimensional cavity are shown in Figure 5.28. The

result shows asymmetric coherent structures similar to the one observed in the wake of a classic bluff bodies such as cylinders.

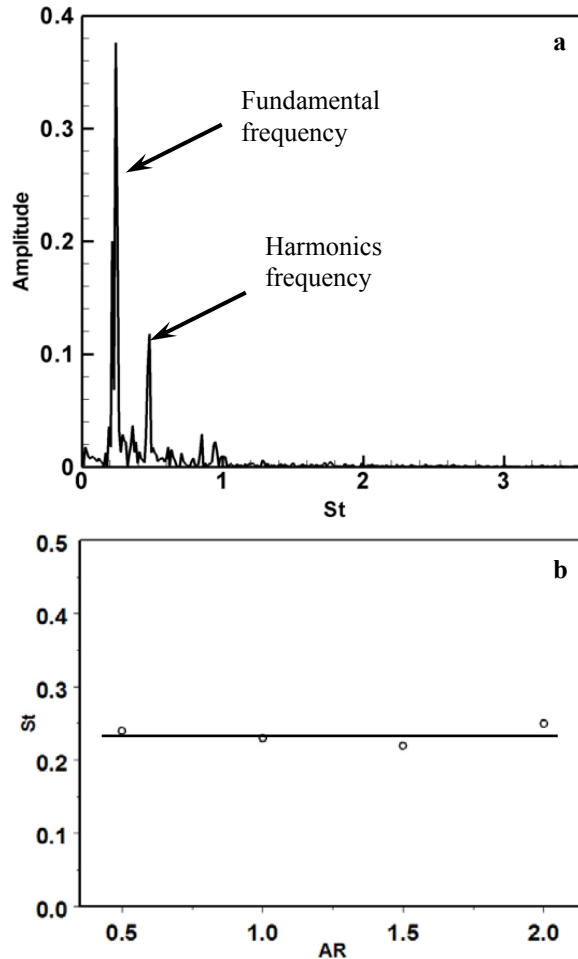


Figure 5.29 a) Power spectrum density of AR = 0.5, b) Strouhal number variations as a function of aspect ratio;  $Re = 7000$ .

Figure 5.29a shows power spectrum density of the wake of aspect ratio 0.5 cavity at Reynolds number of 7000. Two distinct peaks at Strouhal number of 0.24 and 0.48, which correspond to the fundamental and the harmonic frequency of the wakes shedding respectively, are visible in the figure. Other aspect ratios exhibited similar spectral contents. At Reynolds number of 7000, for two-dimensional cavities with different aspect

ratios, the Strouhal numbers of the wakes were found to be 0.24 (Figure 5.29b), which is similar to the one observed in the wake of a cylinder.

### 5.3.2 Effects of Reynolds number

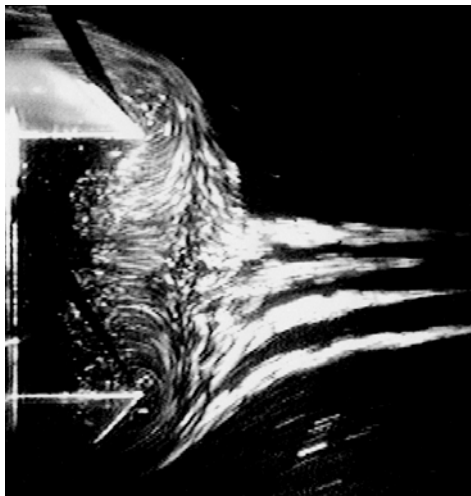


Figure 5.30 Flow visualization image of two-dimensional forward facing cavity; AR = 0.5 and Re = 43000.

Shown in Figure 5.30 is the flow visualization image of a two-dimensional cavity with aspect ratio 0.5 at Reynolds number of 43000. The figure shows the existence of cellular vortical structures similar to the one observed at Reynolds number of 7000. Additionally, flow visualization of various cavity aspect ratios at different Reynolds numbers also showed similar results. This implies that cavity flow kinematics was not Reynolds number dependent. These observations were supported by PIV streamlines plot, two of which are shown in Figure 5.31. Nevertheless, the stability of the vortical structures was observed from the flow visualization results to be affected by Reynolds number. It was observed that an increase in Reynolds number led to increasing vortical structures instability indicated by rapid vortical structures breakdown.

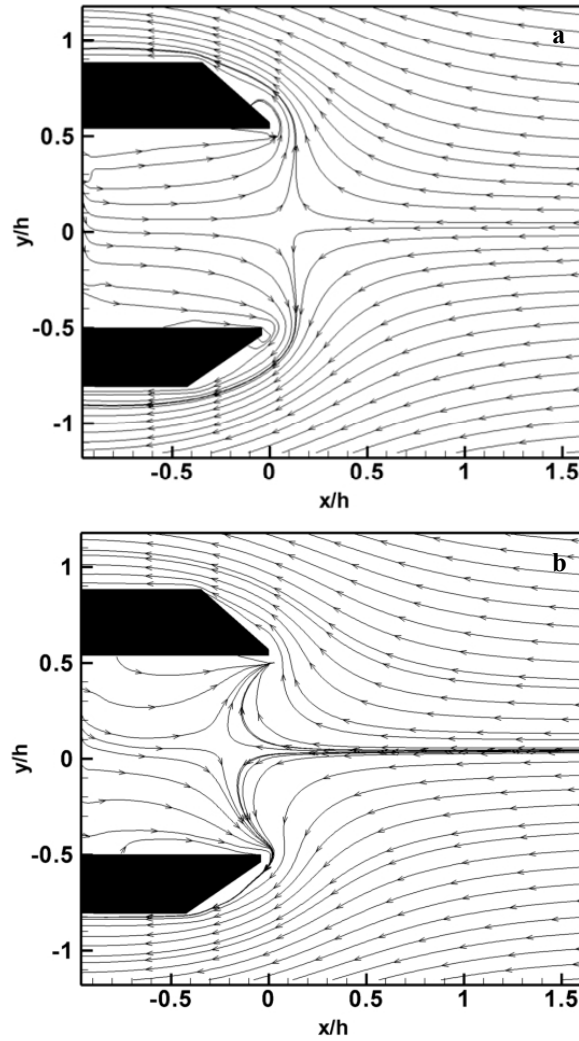


Figure 5.31 Streamline plots of the flowfield of two-dimensional forward facing cavity: a)  $Re = 26000$ , b)  $Re = 43000$ ;  $AR = 1$ .

Both Figure 5.31 and Figure 5.32 show a stream surface that yields singular point. The mean location of the singular point of two-dimensional forward facing cavities of various aspect ratios at different Reynolds numbers is shown in Figure 5.32b. The figure indicates that as Reynolds number increases the singular point tends to stay at the same location,  $x/h = -0.34$ . Similar to the axisymmetric case, for two-dimensional cavity, the effect of aspect ratio to the singular point location is more dominant than Reynolds number.



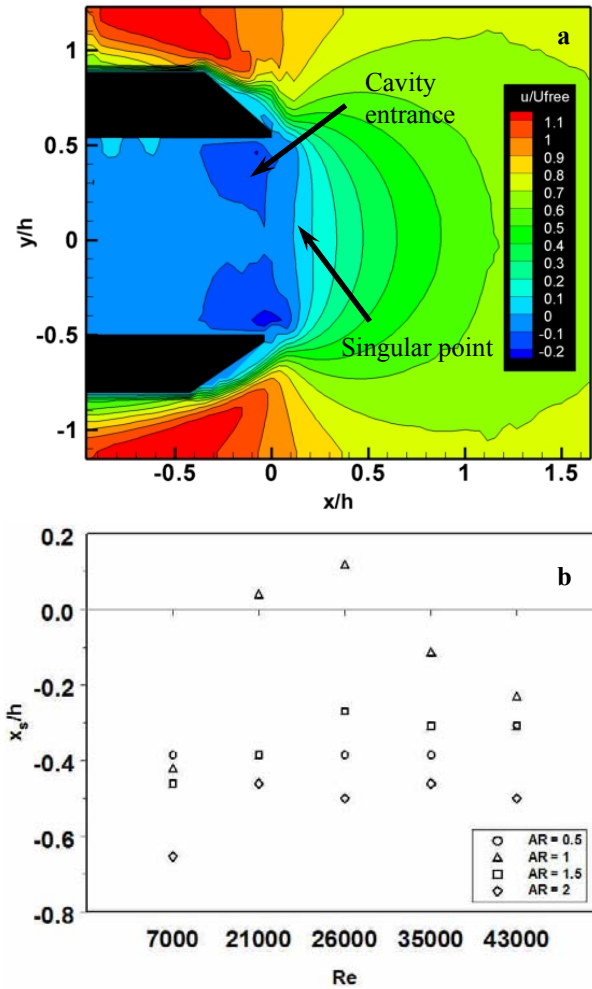


Figure 5.32 a) Nondimensionalized  $u$ -velocity contour map of  $AR = 1$  and  $Re = 26000$ , b) Singular point locations of various aspect ratios at various Reynolds numbers.

The nondimensionalized geometric centerline mean  $u$ -velocity distribution for Aspect ratio of 1.5, with different Reynolds numbers, is shown in Figure 5.33, and indicating a tendency of increasing velocity gradients as the Reynolds number increases. This implies increasing adverse pressure gradients and decreasing pressure relaxation as the Reynolds number increases. Similarly were the case for the other aspect ratios; 0.5, 1 and 2.

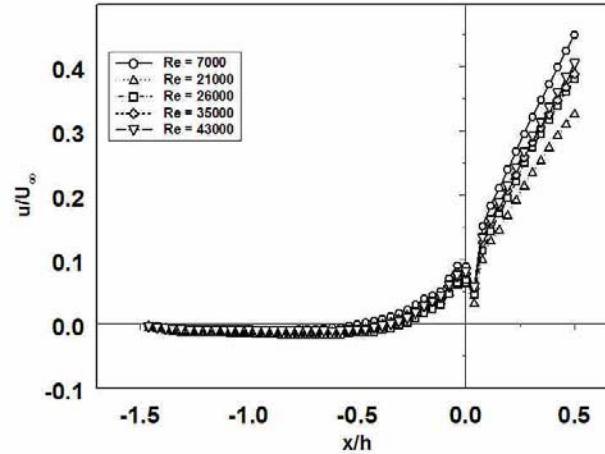


Figure 5.33 Nondimensionalized geometric centerline u-velocity distribution at various Reynolds numbers,  $AR = 1.5$ .

Maximum negative vorticity of reattachment region for various aspect ratios at different Reynolds numbers is shown in Figure 5.32b, and show an increase in vorticity as Reynolds number increases which is a trend similar to with their axisymmetric counterpart. Also observable in Figure 5.32b is that changes in the vorticity of the reattachment region, due to aspect ratio, vary with Reynolds number, which indicates that effects of Reynolds number on vorticity were more dominant than aspect ratio. This observation is in conjunction with previous observation made for axisymmetric cavity.

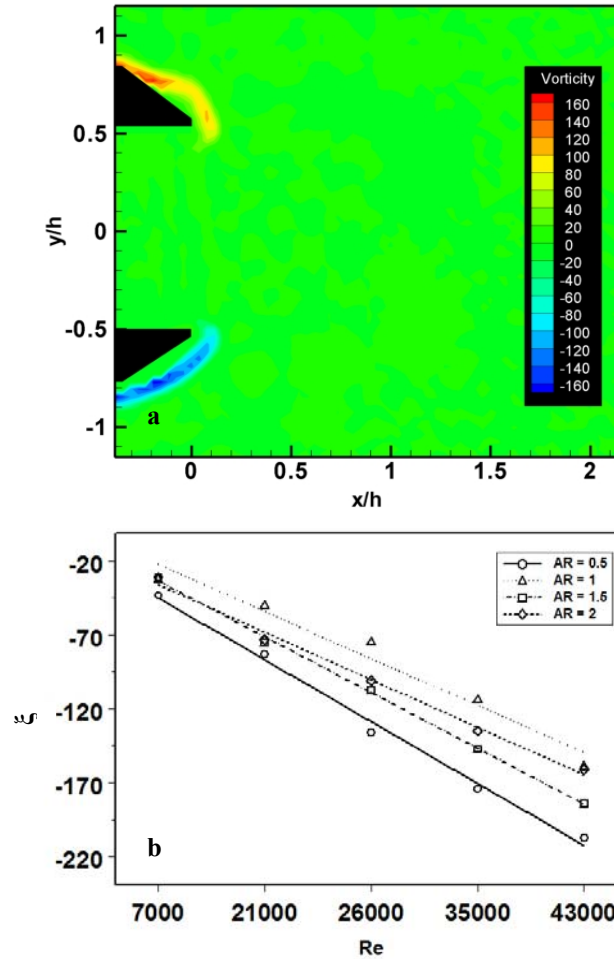


Figure 5.34 a) Vorticity contour of AR = 0.5 and Re = 35000, b) Maximum negative vorticity as a function of Reynolds numbers at various aspect ratios.

Result of spectrum analysis of the wakes of the two-dimensional cavity, with various aspect ratios and at different Reynolds numbers, revealed the existence of subharmonics interactions that became apparent for Reynolds number of 26000 and above. Subharmonics interactions, which indicate merging of eddies with the wake structures, are shown in Figure 5.35a as the peak in the frequency component below the fundamental frequency. Strouhal number of the wake of two-dimensional cavity of

various aspect ratios, at different Reynolds numbers, was found to be 0.21 (Figure 5.35b), and this is a typical Strouhal number of the wake of a classic bluff body.

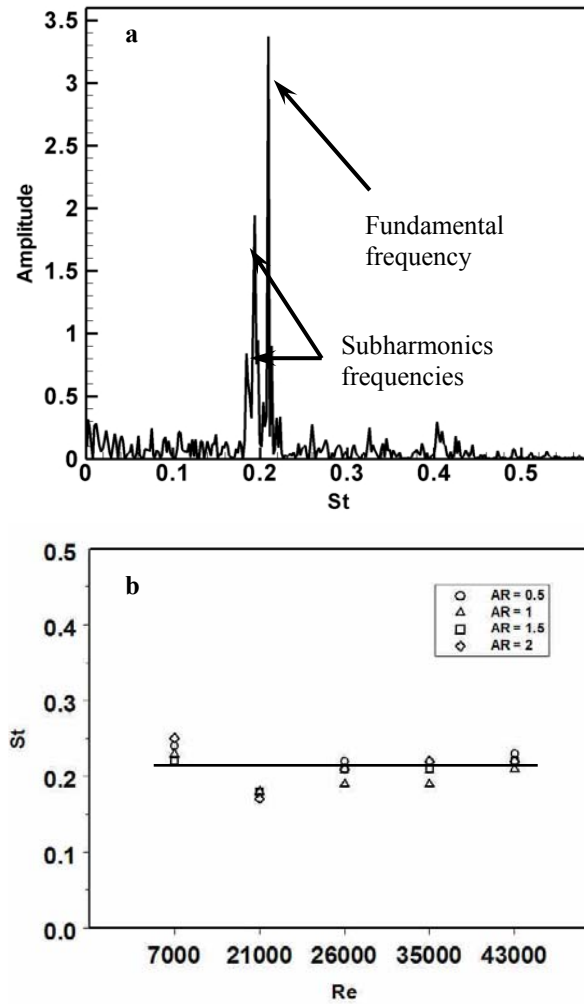


Figure 5.35 a) Power spectrum density of AR = 1 and Re = 43000, b) Strouhal number of various aspect ratios at various Reynolds numbers.

## 6 CONCLUSIONS

Investigations to determine characteristics of the flow around axisymmetric and two-dimensional forward facing cavities were conducted using flow visualization, PIV and CTA. Different cavity aspect ratios; 0.5, 1, 1.5, and 2, were subjected to the tests over a range of Reynolds number; 7000 up to 43000. Analysis of flow visualization results, PIV data and spectral content of hotfilm measurement signals revealed the flow characteristics which can be concluded as the following.

Flow visualization of the axisymmetric cavities revealed the main characteristics of the flow; formation of unstable vortical structures inside the cavity, detached singular point and the ejection of eddy structures. It was observed that the formation of vortical structures and the ejection of eddies were due to the entrainment and exchange between the cavity fluids and the surrounding. Multiple singular points, with the primary being the most upstream one, were observed to develop within the cavity to satisfy flow kinematics. Similar main flow characteristics; formation of unstable vortical structures inside the cavity, detached singular point and the ejection of eddy structures, were also observed for the two-dimensional cavity. Idealized cavity flow topologies, of both axisymmetric and two-dimensional cavities, were developed based on the flow visualization results. Additionally, for axisymmetric cavity, the cavity flow kinematics was found to be independent of the shape of the cavity.

Strong correlations to cavity aspect ratio and Reynolds number were exhibited by both axisymmetric and two-dimensional cavities flow. In the case of axisymmetric cavity, kinematics of the cavity flow was observed to be independent of Reynolds number, However strong dependency to aspect ratio was exhibited by the cavity flow kinematics. This was indicated by an increase in the number of structures formed within the cavity as the aspect ratio increased, which led to greater perturbation on the cavity flow and, consequently, an increase in vortical structures instability. An increase in Reynolds number was also observed to increase vortical structures instability due to increasing unsteadiness in cavity flow. Similar behavior was observed in the vortical structures of the two-dimensional cavity. Nevertheless, kinematics of the cavity flow, in the case of two-dimensional cavity, was observed to be independent of both aspect ratio and Reynolds number.

The primary singular point was observed to move downstream of the cavity interior as the aspect ratio increased for both axisymmetric and two-dimensional cavity. However, in the case of axisymmetric cavity, for  $AR > 1$ , the primary singular point was observed to stay at almost a constant location. For increasing Reynolds number, the primary singular point was found to be at  $x/d = -0.35$  for the axisymmetric cavity, and at  $x/h = -0.34$  for the two-dimensional cavity. This result indicated insensitivity of the primary singular point location to the changes in Reynolds number. Moreover, unsteadiness of the cavity flow structures resulted in the mean location of the primary singular point to be off the geometric centerline.

In the case of axisymmetric cavity, for  $x/d > 0.1$ , adverse pressure gradient inferred from the velocity gradient was observed to be a function of Reynolds number but not of aspect ratio, and the conversely was true for  $x/d < 0.1$ . However, for two-dimensional cavity, the adverse pressure gradient only indicated strong correlations to Reynolds number. Additionally, vorticity in the flowfield of forward facing cavity, for both axisymmetric and two-dimensional, was observed to be more affected by changes in Reynolds number.

Spectrum analysis of the wake of axisymmetric cavity indicated strong correlations between the wake and the upstream flow. It was observed that the asymmetric shedding of the wake imposed subharmonics disturbances on the upstream flow which resulted in periodic ejection of the fluid structures from the cavity. Also, the wake of axisymmetric cavities was observed to be dependent of the aspect ratio of the cavity. This was indicated by increasing Strouhal number with the aspect ratio, which also implied an increase in disturbances imposed on the upstream flow and, consequently, instability of the flow structures inside the cavity.

Furthermore, spectrum analysis of the wake of two-dimensional cavities showed the existence of both harmonics which indicated the breaking of eddy structures, and subharmonics interactions which indicated merging of eddy structures. The subharmonics interactions were observed to be more prominent at high Reynolds number. Additionally, the Strouhals frequency of the wakes of two-dimensional cavity was found to be 0.21, which is a common value for the wakes of classic bluff body such as cylinder.

## REFERENCES

- <sup>1</sup> Auman, L. M., Dahlke, C. W., and Purinton, D. C., "Aerodynamic Characteristics of Ribbon Stabilized Grenades," AIAA Aerospace Sciences Meeting and Exhibit, AIAA, Reston, VA, 2000.
- <sup>2</sup> Biswas, G., and Eswaran, V. (ed.), *Turbulent Flows Fundamentals, Experiments and Modeling*, Alpha Science, Pangbourne, England, UK, 2002.
- <sup>3</sup> Huerre, P., and Monkewitz, P. A., "Local and Global Instabilities in Spatially Developing Flows," *Ann. Rev. Fluid Mech.*, Vol. 22, 1990, pp. 473-531.
- <sup>4</sup> Anderson, J. D., *Fundamental of Aerodynamics*, 2nd ed., McGraw-Hill, Singapore, 1991.
- <sup>5</sup> Smith, M. C., "Wake-Induced Effects near the Forward Stagnation Point of a Circular Cylinder," *Phys. of Fluids*, Vol. 11, No. 9, 1968, pp. 1618-1620.
- <sup>6</sup> Piercy, N., and Richardson, E., *Aeronautical Research Council Reports and Memoranda*, 1928, pp 1224.
- <sup>7</sup> Kuethe, A., Willmarth, W. and Crocker, G., "Stagnation Point Fluctuations on a Body of Revolution," *Phys. of Fluids*, Vol. 2, 1959, pp. 714-716.



- <sup>8</sup> Lamberson, D., Higuchi, H., and VanRooij, M., "Characteristics of Flow within Concave-Nosed Bodies," AIAA Aerodynamic Decelerator Systems Technology Conference, AIAA, Reston, VA, 1999, pp. 279-287.
- <sup>9</sup> Bastianon, R., "Unsteady Solution of the Flowfield over Concave Bodies," AIAA Journal, Vol. 7, No. 3, 1969, pp. 531-533.
- <sup>10</sup> Dorrepaal, J. M., O'Neill, M. E., and Ranger, K. B., "Axisymmetric Stokes Flow Past a Spherical Cap," J. Fluid Mech., Vol. 75, No. 2, 1976, pp. 273-286.
- <sup>11</sup> Higuchi, H., and Takahashi, F., "Flow Past Two-Dimensional Ribbon Parachute Models," J. Aircraft, Vol. 26, No. 7, 1989, pp. 641-649.
- <sup>12</sup> Higuchi, H., "Visual Study on Wakes Behind Solid and Slotted Axisymmetric Bluff Bodies," J. Aircraft, Vol. 28, No. 7, 1991, pp. 427-430.
- <sup>13</sup> Johari, H., and Desabrais, K. J., "Vortex Shedding in the near Wake of Parachute Canopy," J. Fluid Mech., Vol. 536, 2005, pp. 185-207.
- <sup>14</sup> Engblom, W. A., Yüceil, B., Goldstein, D. B., and Dolling, D. S., "Experimental and Numerical Study of Hypersonic Forward-Facing Cavity Flow," J. Spacecraft and Rockets, Vol. 33, No. 3, 1996, pp. 353-359.
- <sup>15</sup> Yüceil, B., and Dolling, D. S., "Infrared Imaging and Shock Visualization of Flow over Concave Blunt Bodies," J. Thermophysics and Heat Transfer, Vol. 11, No. 3, 1997, pp. 375-383.

- <sup>16</sup> Huebner, L. D., and Utereja, L. R., "Mach 10 Bow-Shock Behaviour of a Forward Facing Nose Cavity," *J. Spacecraft and Rockets*, Vol. 30, No. 3, 1993, pp. 291-297.
- <sup>17</sup> Smits, A. J., and Lim, T. T. (ed.), *Flow Visualization Techniques and Examples*, Imperial College, Singapore, 2000.
- <sup>18</sup> Gharib, M. and Willert, C. E., "Digital Particle Image Velocimetry," *Experiments in Fluids*, Vol. 10, 1991, pp. 181-193.
- <sup>19</sup> Hunt, J. C. R., Abell, C. J., Peterka, J. A., and Woo, H., "Kinematical Studies of the Flows around Free or Surface-Mounted Obstacles; Applying Topology to Flow Visualization," *J. Fluid Mech.*, Vol. 86, No.1, 1978, pp. 179-200.
- <sup>20</sup> Dahlke, C. W., "Aerodynamics and Flight Dynamics of Ribbon Stabilized Grenades," *AIAA Aerospace Sciences Meeting*, AIAA, New York, 1979.
- <sup>21</sup> Dahlke, C. W., and Auman, L. M., "Drag Characteristics of Ribbons," *AIAA Aerodynamics Decelerator Systems Technology Conference*, AIAA, Reston, VA, 2001.
- <sup>22</sup> Auman, L. M., and Wilks, B. L., "Application of Fabric Ribbons for Drag and Stabilization," *AIAA Aerodynamics Decelerator Systems Technology Conference*, AIAA, Reston, VA, 2005.
- <sup>23</sup> Siltou, S. I., and Goldstein, D. B., "Ablation Onset in Unsteady Hypersonic Flow About Nose Tip with Cavity," *J. Thermophysics and Heat Transfer*, Vol. 14, No. 3, 2000, pp. 421-434.

- <sup>24</sup> Achenbach, E., "Vortex Shedding from Spheres," *J. Fluid Mech.*, Vol. 62, No. 2, 1974, pp. 209-221.
- <sup>25</sup> Taneda, S., "Visual Observations of the Flow Past a Sphere at Reynolds Numbers 104 and 106," *J. Fluid Mech.*, Vol. 85, No. 1, 1978, pp. 187-192.
- <sup>26</sup> Fuchs, H. V., Mercker, E., and Michel, U., "Large-Scale Coherent Structures in the Wake of Axisymmetric Bodies," *J. Fluid Mech.*, Vol. 93, No. 1, 1979, pp. 185-207.
- <sup>27</sup> Monkewitz, P. A., "A Note on Vortex Shedding from Axisymmetric Bluff Bodies," *J. Fluid Mech.*, Vol. 192, 1988, pp. 561-575.
- <sup>28</sup> Berger, E., Scholz, D., and Schumm, M., "Coherent Vortex Structures in the Wake of a Sphere and a Circular disk at Rest and under Forced Vibrations," *J. Fluids and Structures*, Vol. 4, 1990, pp. 231-257.
- <sup>29</sup> Natarajan, R., and Acrivos, A., "The Instability of the Steady flow Past Spheres and Disks," *J. Fluid Mech.*, Vol. 254, 1993, pp. 323-344.
- <sup>30</sup> Sakamoto, H., and Haniu, H., "The Formation mechanism and Shedding Frequency of Vortices from a Sphere in Uniform Shear Flow," *J. Fluid Mech.*, Vol. 287, 1995, pp. 151-171.
- <sup>31</sup> Griffin, O. M., and Hall, M. S., "Vortex Shedding and Lock-On in Bluff Body Wakes," *Int. Symposium on Nonsteady Fluid Dynamics*, ASME, New York, 1990, pp. 209-218.

## **APPENDICES**

## **Appendix A: Effect of the bubble probes**

The differences between results of the stand alone PLIF flow visualization and the combination of PLIF and hydrogen bubbles raised a question of results validation. Hence, PIV was used to validate flow visualization results. Two flow conditions were used, they were undisturbed (no bubble wire presence) and disturbed (with bubble wire upstream of the cavity) oncoming flow. The results are shown in Figure A. 1.

Figure A. 1a shows the mean velocity vector map of the cavity flow and it shows the reversed oncoming flow near cavity entrance and also the nearly stagnant fluid near the base of the cavity. This result explains why the cavity flow pattern was not observable in stand alone PLIF flow visualization. In Figure A. 1b however, both secondary and primary structures in their unstable state, where weaker structures were already ejected, were shown. These differences were conjectured due to the differences in the level of kinetic energy of the oncoming fluid particles. For undisturbed condition, the oncoming fluid particle did not have enough kinetic energy to significantly induce velocity onto the nearly stagnant fluid inside the cavity. However, the presence of bubble wire, upstream of the model, added more disturbances to the oncoming flow which resulted in additional kinetic energy. This additional kinetic energy caused disturbed oncoming flow to be able to induce velocity significant enough to create primary and secondary structures, and consequently cavity flow pattern became discernible. In

addition, the differences between the cavity flow patterns of the undisturbed and disturbed oncoming flows show that forward facing cavity flow was very sensitive to upstream disturbances, and that just a slight disturbance was enough to excite cavity fluid particles and induce instability.

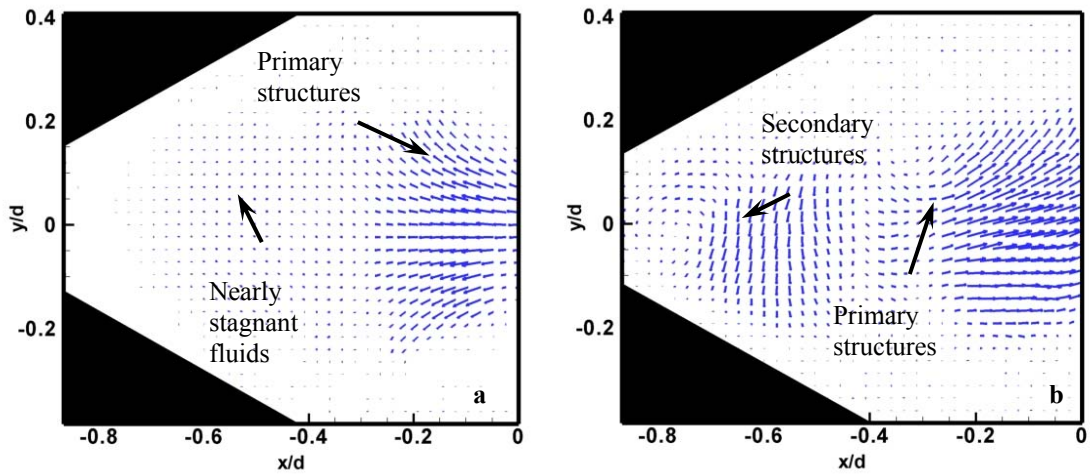


Figure A. 1 Cavity flow mean velocity vector map; a) undisturbed, b) disturbed.

## Appendix B: Flow visualizations

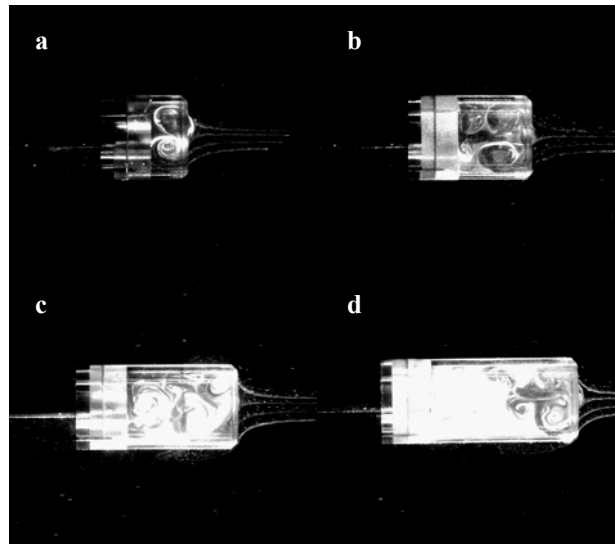


Figure B. 1 Flow visualizations of axisymmetric cavity at  $Re = 7000$ : a)  $AR = 0.5$ , b)  $AR = 1$ ,  $AR = 1.5$ , c)  $AR = 2$ .

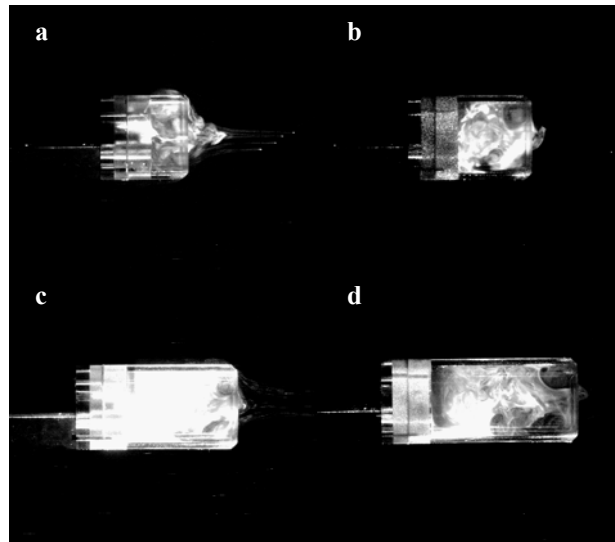


Figure B. 2 Flow visualizations of axisymmetric cavity at  $Re = 21000$ : a)  $AR = 0.5$ , b)  $AR = 1$ ,  $AR = 1.5$ , c)  $AR = 2$ .

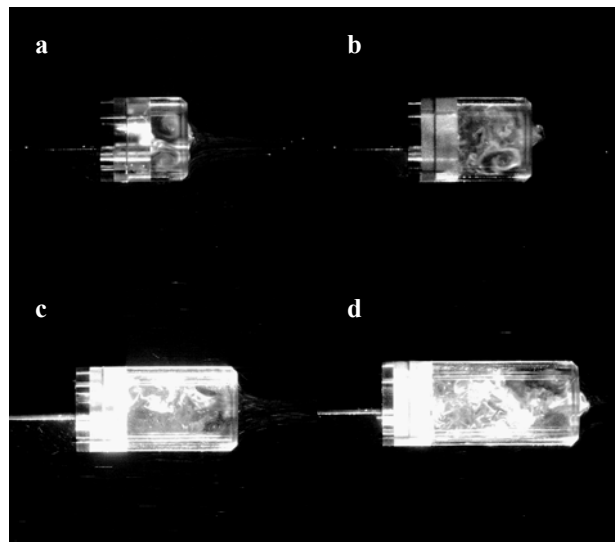


Figure B. 3 Flow visualizations of axisymmetric cavity at  $Re = 26000$ : a)  $AR = 0.5$ , b)  $AR = 1$ ,  $AR = 1.5$ , c)  $AR = 2$ .



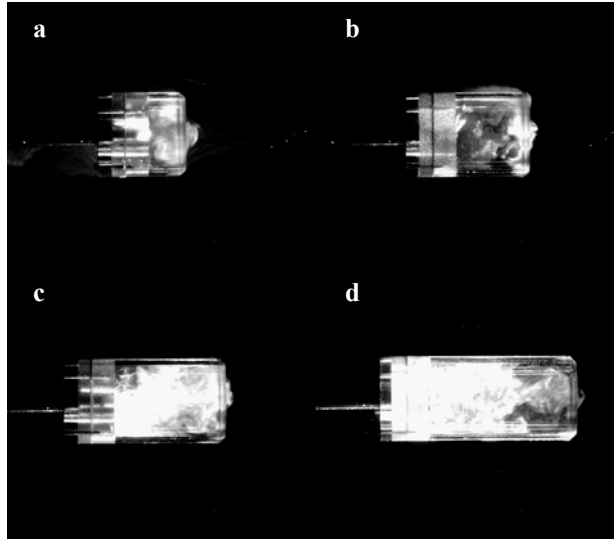


Figure B. 4 Flow visualizations of axisymmetric cavity at  $Re = 35000$ : a)  $AR = 0.5$ , b)  $AR = 1$ ,  $AR = 1.5$ , c)  $AR = 2$ .

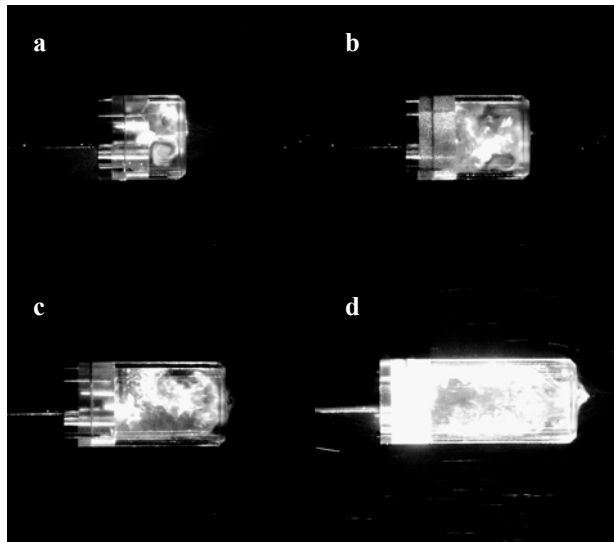


Figure B. 5 Flow visualizations of axisymmetric cavity at  $Re = 43000$ : a)  $AR = 0.5$ , b)  $AR = 1$ ,  $AR = 1.5$ , c)  $AR = 2$ .

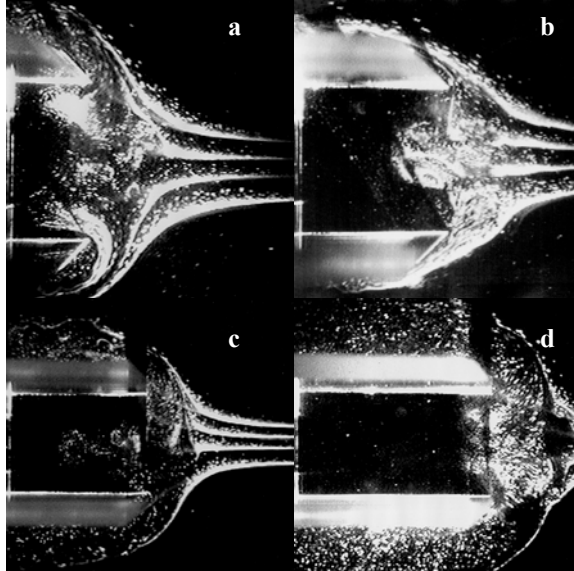


Figure B. 6 Flow visualizations of two-dimensional cavity at  $Re = 7000$ :  
a)  $AR = 0.5$ , b)  $AR = 1$ ,  $AR = 1.5$ , c)  $AR = 2$ .

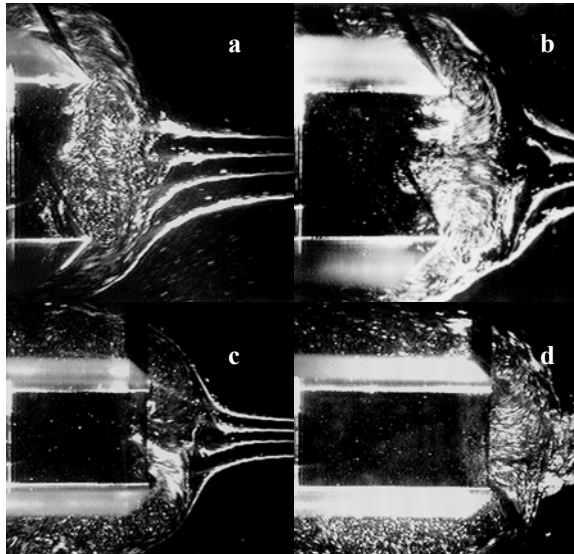


Figure B. 7 Flow visualizations of two-dimensional cavity at  $Re = 21000$ : a)  $AR = 0.5$ , b)  $AR = 1$ ,  $AR = 1.5$ , c)  $AR = 2$ .

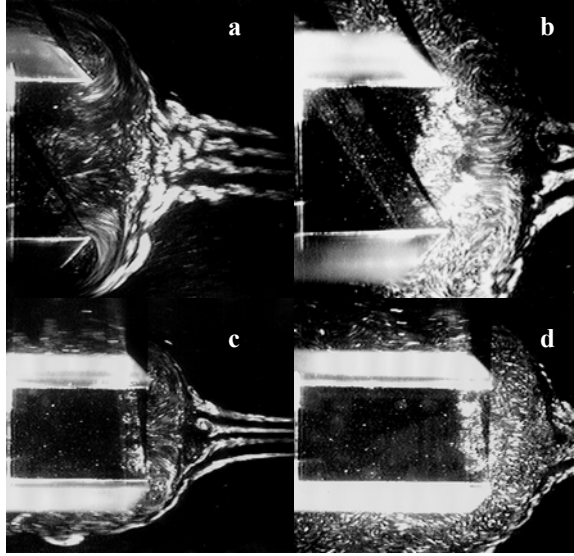


Figure B. 8 Flow visualizations of two-dimensional cavity at  $Re = 26000$ : a)  $AR = 0.5$ , b)  $AR = 1$ ,  $AR = 1.5$ , c)  $AR = 2$ .

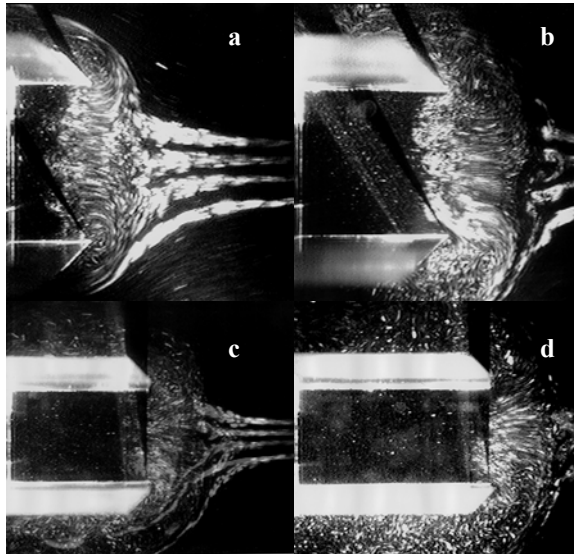


Figure B. 9 Flow visualizations of two-dimensional cavity at  $Re = 35000$ : a)  $AR = 0.5$ , b)  $AR = 1$ ,  $AR = 1.5$ , c)  $AR = 2$ .

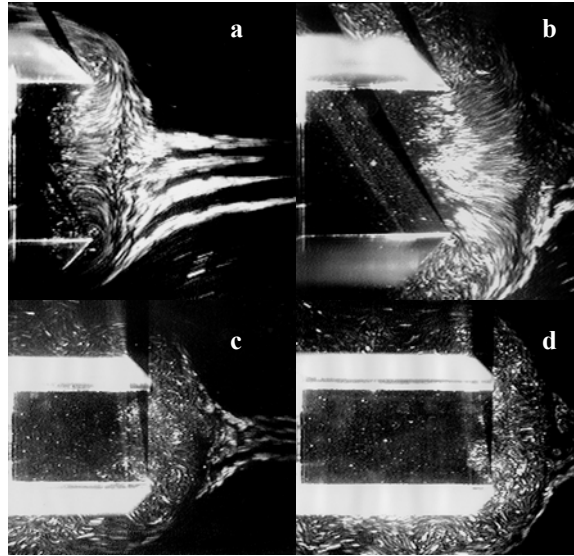


Figure B. 10 Flow visualizations of two-dimensional cavity at  $Re = 43000$ : a)  $AR = 0.5$ , b)  $AR = 1$ ,  $AR = 1.5$ , c)  $AR = 2$ .

## Appendix C: Streamlines

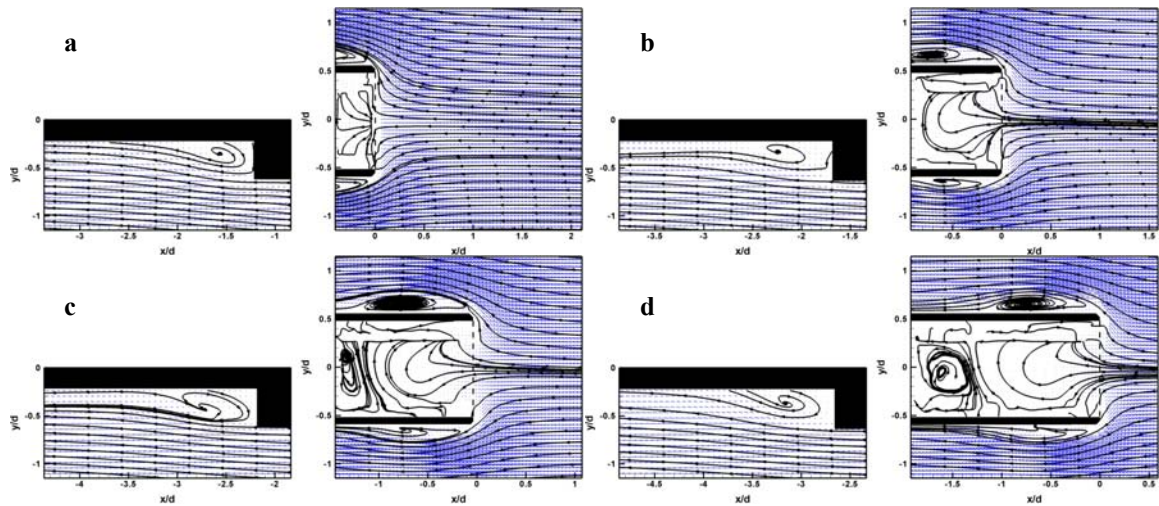


Figure C. 1 Streamlines around the axisymmetric cavity at  $Re = 7000$ : a)  $AR = 0.5$ , b)  $AR = 1$ ,  $AR = 1.5$ , c)  $AR = 2$ .

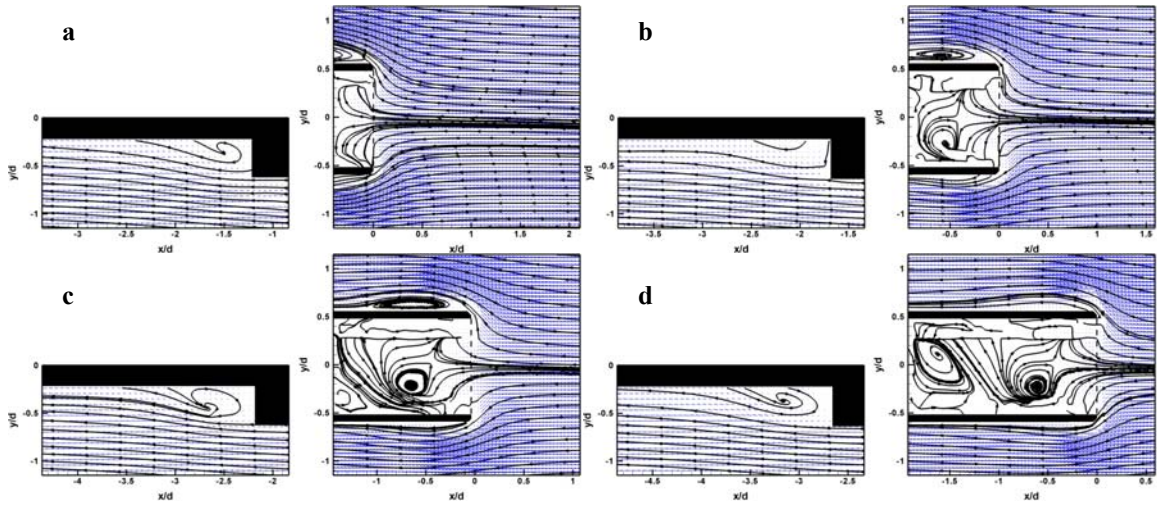


Figure C. 2 Streamlines around the axisymmetric cavity at  $Re = 21000$ : a)  $AR = 0.5$ , b)  $AR = 1$ ,  $AR = 1.5$ , c)  $AR = 2$ .

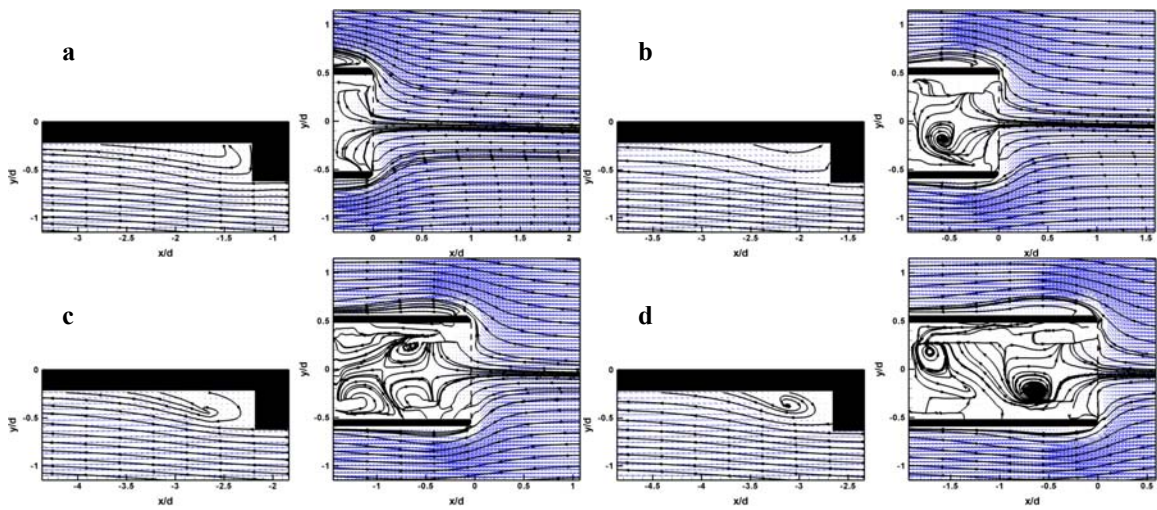


Figure C. 3 Streamlines around the axisymmetric cavity at  $Re = 26000$ : a)  $AR = 0.5$ , b)  $AR = 1$ ,  $AR = 1.5$ , c)  $AR = 2$ .

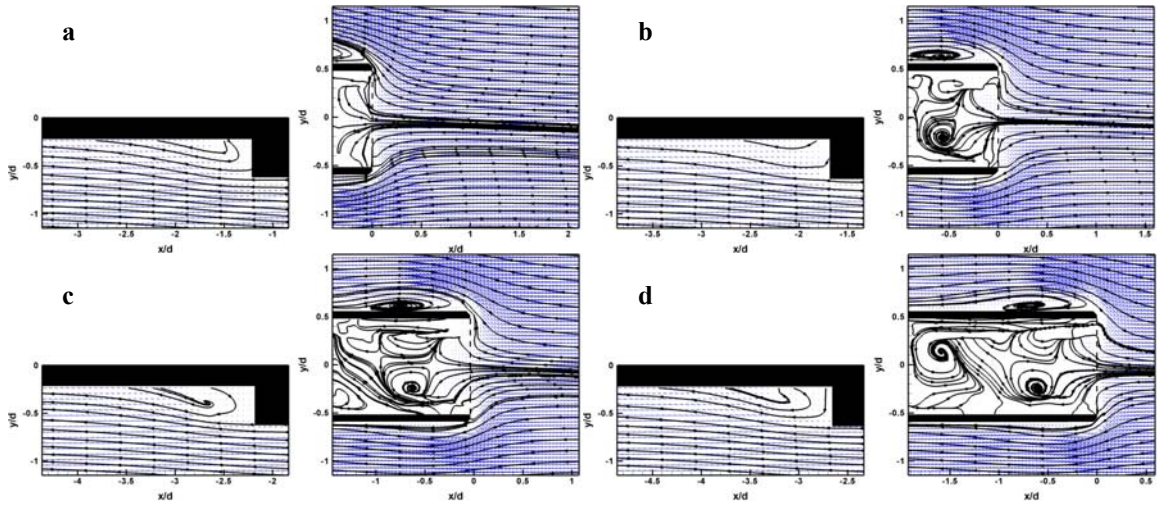


Figure C. 4 Streamlines around the axisymmetric cavity at  $Re = 35000$ : a)  $AR = 0.5$ , b)  $AR = 1$ ,  $AR = 1.5$ , c)  $AR = 2$ .

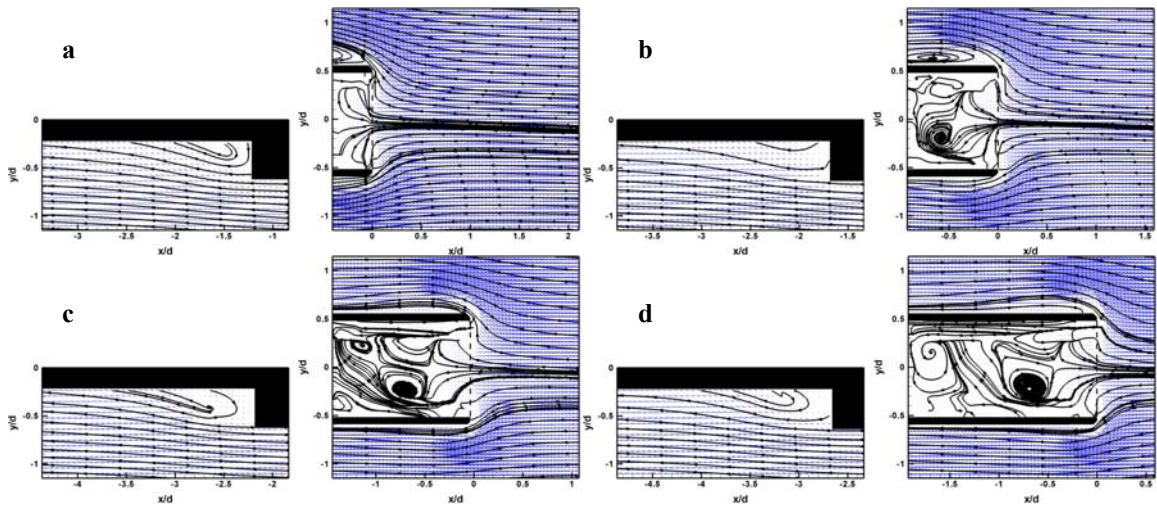


Figure C. 5 Streamlines around the axisymmetric cavity at  $Re = 43000$ : a)  $AR = 0.5$ , b)  $AR = 1$ ,  $AR = 1.5$ , c)  $AR = 2$ .

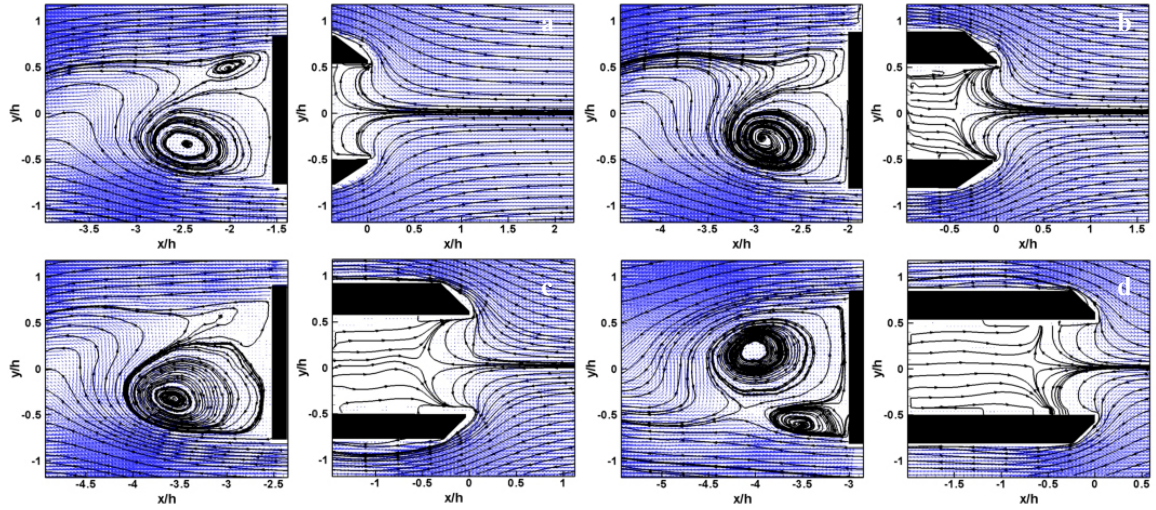


Figure C. 6 Streamlines around the two-dimensional cavity at  $Re = 7000$ : a)  $AR = 0.5$ , b)  $AR = 1$ ,  $AR = 1.5$ , c)  $AR = 2$ .

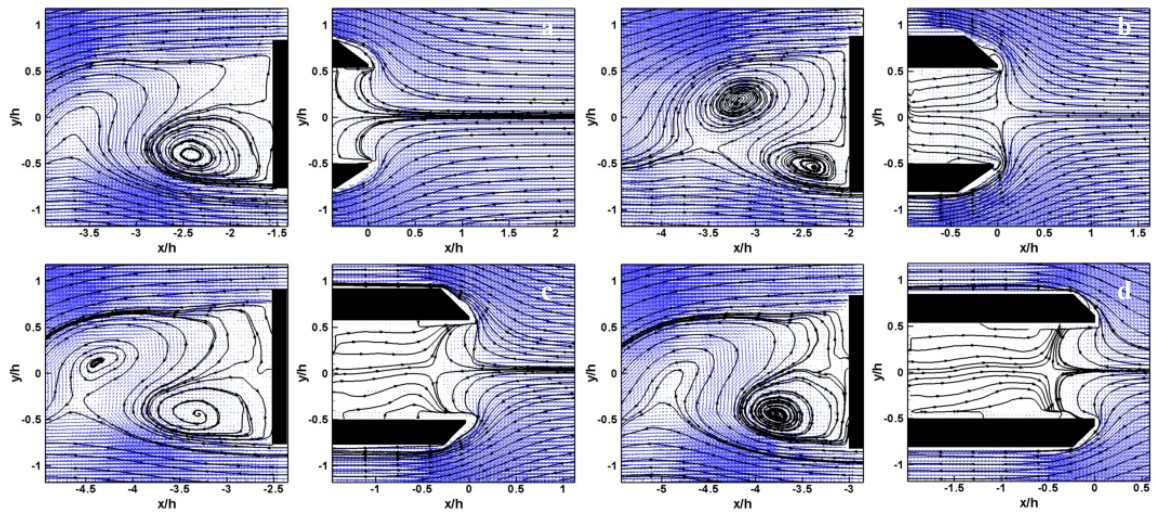


Figure C. 7 Streamlines around the two-dimensional cavity at  $Re = 21000$ : a)  $AR = 0.5$ , b)  $AR = 1$ ,  $AR = 1.5$ , c)  $AR = 2$ .



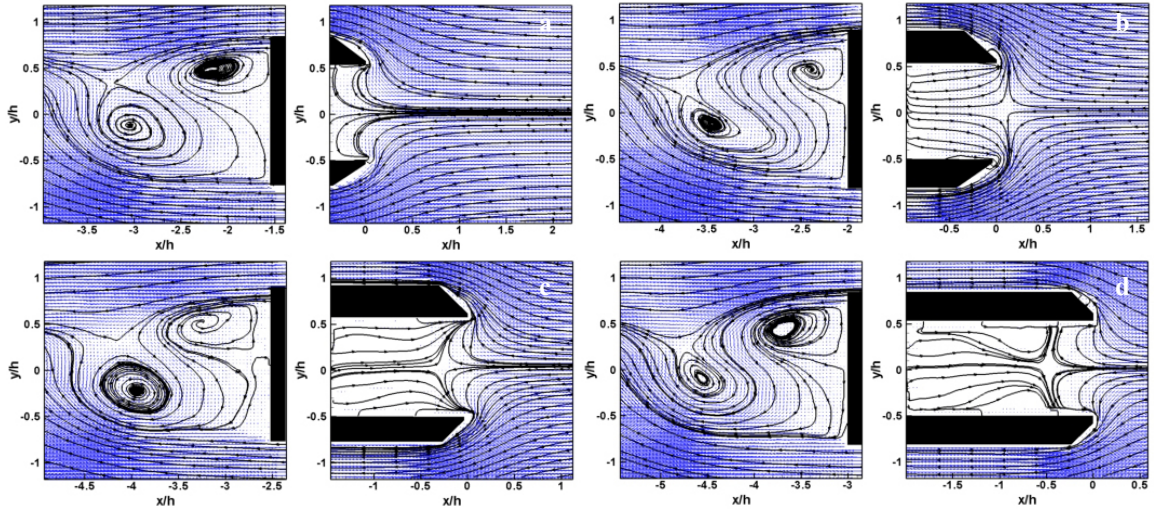


Figure C. 8 Streamlines around the two-dimensional cavity at  $Re = 26000$ : a)  $AR = 0.5$ , b)  $AR = 1$ ,  $AR = 1.5$ , c)  $AR = 2$ .

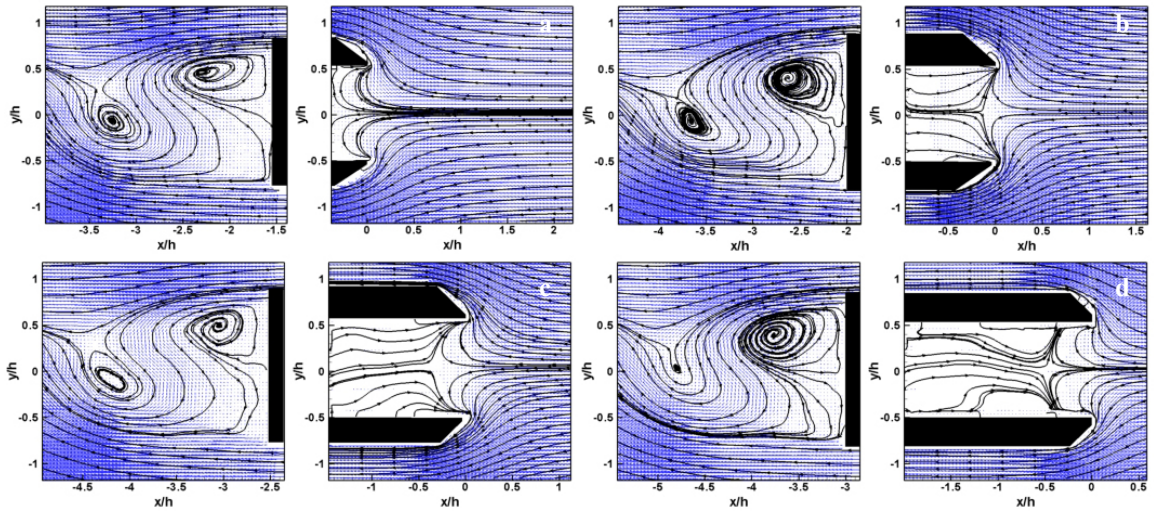


Figure C. 9 Streamlines around the two-dimensional cavity at  $Re = 35000$ : a)  $AR = 0.5$ , b)  $AR = 1$ ,  $AR = 1.5$ , c)  $AR = 2$ .

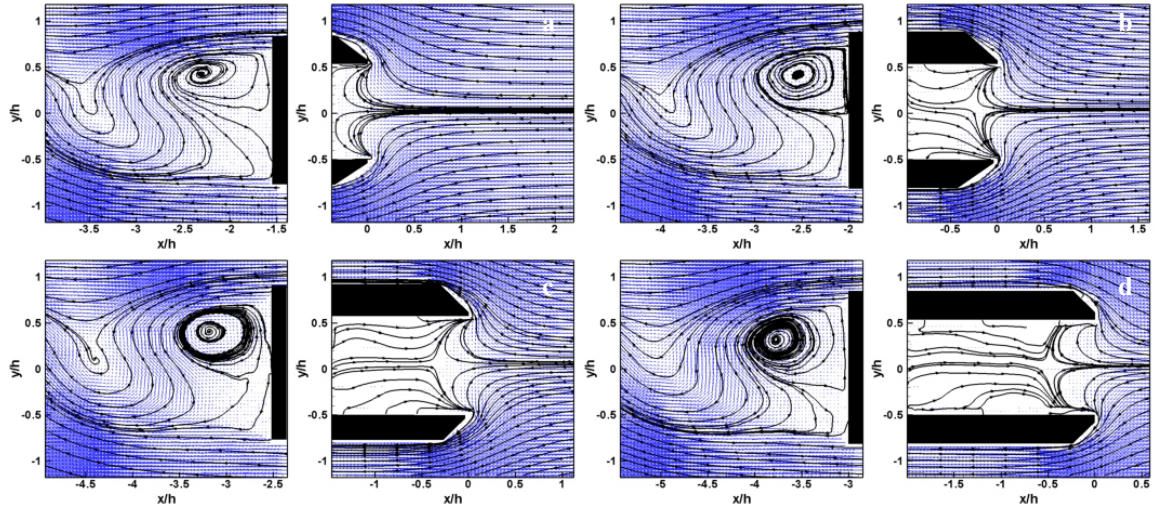


Figure C. 10 Streamlines around the two-dimensional cavity at  $Re = 43000$ : a)  $AR = 0.5$ ,  
 b)  $AR = 1$ ,  $AR = 1.5$ , c)  $AR = 2$ .